

CFD Applications and Validations in Aerodynamic Design and Analysis for Missiles

Kwang Seop Lee
Seung Kyu Hong

Korea
Agency for Defense Development
Taejon, 305-600
Email address ks1959@yahoo.com, dskhong@yahoo.com

Abstract

CFD examples at ADD are introduced to show their variety at its application in the course of a missile design. Four examples are an ogive-cylinder and boat tail, nose spike, vertical launcher internal and side jet interaction flows at supersonic flow region. Various means of validation for those complex flows are also described. This paper is thus intended to show how CFD and its validation share their role at the ADD aerodynamic research laboratory.

Key words: missile design, jet impingement, vertical launching system, side jet, etc.

1. Introduction

In the course of a missile system design, generation of aerodynamic performance data comes first to scale the configuration. For this activity a standard empirical or semi-empirical code is utilized to generate a quick performance data. Due to the disparity between the input geometry for these empirical codes and the real flow conditions or the geometry, wind tunnel testing is done to supplement the aerodynamic data for evaluation of flight simulation. However, there are other situations which demand a detailed flow simulation for phenomenological understanding. Cases in point are supersonic missile body flow at high angle of attack, boat tail and spike design, jet impingement from rocket plume on an opposing wall, and side jet interactions over a supersonic missile. In this introductory paper, a few examples for CFD applications that are encountered during the missile design are given along with validation methods for the computed results.

Numerical study of the jet flow is carried out using a three-dimensional Navier-Stokes solver incorporating the Characteristic Flux Difference Splitting (CFDS) method [1]. CFDS method, a variant of Roe's flux-difference splitting formulation, has been developed formerly as a viable engineering prediction tool for aerodynamic design and had indeed shown its versatility in computing complex flows [2]. The CFDS method, however, being rooted from Roe's flux-difference is also susceptible to the carbuncle problem. This shock instability problem has been cured and the code is then applied to many shock/boundary interaction situations cited herein.

2. Numerical Method

The Characteristic Flux Difference Splitting (CFDS), numerical method for the three-dimensional Navier-Stokes has been applied to various complex flows and validated over the past few years [1]. The governing Navier-Stokes equations employed in the generalized coordinate system (ξ, η, ϕ) are expressed for the conservative variable vector as

$$J^{-1} \frac{\partial \mathbf{Q}}{\partial t} + \frac{\partial}{\partial \xi} (\hat{\mathbf{F}} + \hat{\mathbf{F}}_v) + \frac{\partial}{\partial \eta} (\hat{\mathbf{G}} + \hat{\mathbf{G}}_v) + \frac{\partial}{\partial \phi} (\hat{\mathbf{H}} + \hat{\mathbf{H}}_v) = 0 \quad (1)$$

Report Documentation Page				Form Approved OMB No. 0704-0188	
Public reporting burden for the collection of information is estimated to average 1 hour per response, including the time for reviewing instructions, searching existing data sources, gathering and maintaining the data needed, and completing and reviewing the collection of information. Send comments regarding this burden estimate or any other aspect of this collection of information, including suggestions for reducing this burden, to Washington Headquarters Services, Directorate for Information Operations and Reports, 1215 Jefferson Davis Highway, Suite 1204, Arlington VA 22202-4302. Respondents should be aware that notwithstanding any other provision of law, no person shall be subject to a penalty for failing to comply with a collection of information if it does not display a currently valid OMB control number.					
1. REPORT DATE JUN 2007		2. REPORT TYPE N/A		3. DATES COVERED -	
4. TITLE AND SUBTITLE CFD Applications and Validations in Aerodynamic Design and Analysis for Missiles				5a. CONTRACT NUMBER	
				5b. GRANT NUMBER	
				5c. PROGRAM ELEMENT NUMBER	
6. AUTHOR(S)				5d. PROJECT NUMBER	
				5e. TASK NUMBER	
				5f. WORK UNIT NUMBER	
7. PERFORMING ORGANIZATION NAME(S) AND ADDRESS(ES) Korea Agency for Defense Development Taejon, 305-600				8. PERFORMING ORGANIZATION REPORT NUMBER	
9. SPONSORING/MONITORING AGENCY NAME(S) AND ADDRESS(ES)				10. SPONSOR/MONITOR'S ACRONYM(S)	
				11. SPONSOR/MONITOR'S REPORT NUMBER(S)	
12. DISTRIBUTION/AVAILABILITY STATEMENT Approved for public release, distribution unlimited					
13. SUPPLEMENTARY NOTES Third International Symposium on Integrating CFD and Experiments in Aerodynamics, June 2007, The original document contains color images.					
14. ABSTRACT					
15. SUBJECT TERMS					
16. SECURITY CLASSIFICATION OF:			17. LIMITATION OF ABSTRACT UU	18. NUMBER OF PAGES 56	19a. NAME OF RESPONSIBLE PERSON
a. REPORT unclassified	b. ABSTRACT unclassified	c. THIS PAGE unclassified			

where \mathbf{J}^{-1} is the Jacobian of the transformation, \mathbf{Q} is the conservative variable vector, $\hat{\mathbf{F}}, \hat{\mathbf{G}}$ and $\hat{\mathbf{H}}$ are inviscid flux vectors, and, $\hat{\mathbf{F}}_v, \hat{\mathbf{G}}_v$ and $\hat{\mathbf{H}}_v$ are viscous flux vectors. The inviscid fluxes are linearized and split for upwind discretizations by

$$\Delta_\xi \mathbf{F} = \tilde{\mathbf{A}} \Delta \mathbf{Q} = (\tilde{\mathbf{A}}^+ + \tilde{\mathbf{A}}^-) \Delta \mathbf{Q} \quad \text{and} \quad \tilde{\mathbf{A}}^\pm = \overline{\mathbf{M}} \overline{\mathbf{T}} \Lambda^\pm \overline{\mathbf{M}}^{-1} \overline{\mathbf{T}}^{-1} \quad (2)$$

yielding

$$\mathbf{J}^{-1} \frac{\delta \mathbf{Q}}{\Delta t} + \tilde{\mathbf{A}}^+ \nabla_\xi \mathbf{Q} + \tilde{\mathbf{A}}^- \Delta_\xi \mathbf{Q} + \tilde{\mathbf{B}}^+ \nabla_\eta \mathbf{Q} + \tilde{\mathbf{B}}^- \Delta_\eta \mathbf{Q} + \tilde{\mathbf{C}}^+ \nabla_\phi \mathbf{Q} + \tilde{\mathbf{C}}^- \Delta_\phi \mathbf{Q} = 0 \quad (3)$$

where $\delta \mathbf{Q} = \mathbf{Q}^{(n+1)} - \mathbf{Q}^{(n)}$ and the overbar means the associated variable is space-averaged over the interval, [j, j+1]. $\overline{\mathbf{M}}$ or $\overline{\mathbf{M}}^{-1}$ is a transformation matrix between the conservative variable vector \mathbf{Q} and the primitive variable vector, $\tilde{\mathbf{Q}}$. $\overline{\mathbf{T}}$ or its inverse $\overline{\mathbf{T}}^{-1}$ is defined to be a transformation matrix between the primitive variable vector $\tilde{\mathbf{Q}}$ and the characteristic variable vector, $\tilde{\tilde{\mathbf{Q}}}$.

In the case of supersonic jet impingement calculations, the entropy fixing formula employed are

$$|\lambda| = \left(\frac{\lambda^2 + \varepsilon^2}{2\varepsilon} \right) \quad \text{if} \quad |\lambda| < \varepsilon \quad (4)$$

with ε = constant to prevent shock instability problem.

3. CFD Applications in Aerodynamic Design and Analysis

3.1 Supersonic Ogive-cylinder

Supersonic flow past an ogive-cylinder with the secant ogive of 3-caliber length is run for Mach 3 with $\alpha = 10.0^\circ$ and $\text{Re} = 6 \times 10^6$ [3]. Degani-Schiff [4] turbulent model, modified from Baldwin-Lomax model, was used since the flow involves cross flow separation at high angle of attack. Pressure distributions on the upper and lower surface along the longitudinal body are compared with experimental data [3] in Fig. 1 with a good match even with 1st-order differencing. Although 1st-order solution follows the experimental trend pretty well, the second-order spatial accuracy improves the quality of the solution as is apparent from Fig. 2 which compares circumferential pressure distributions at $x = 5.77$ caliber location.

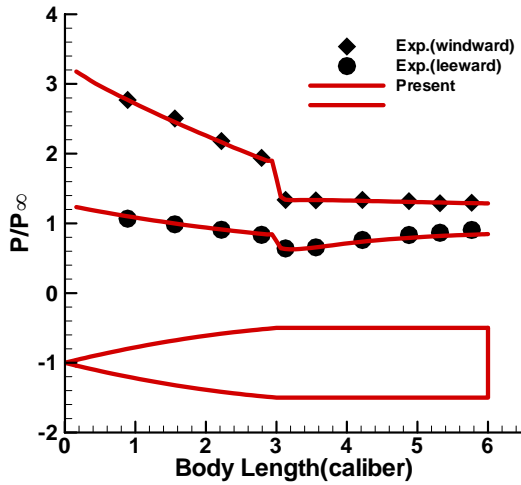


Figure 1. Jet Surface pressure distribution over an ogive at $M=3.0$, $\alpha=10.0^\circ$.

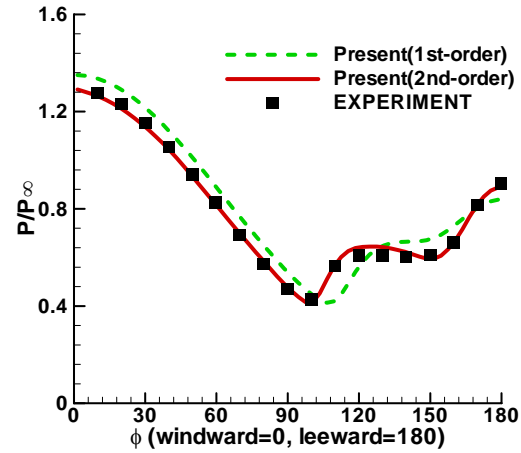


Figure 2. Circumferential pressure distribution at $x=5.77D$ for $M=3.0$, $\alpha=10.0^\circ$.

3.2 Boat Tail Configuration Design and Nose Spike Design

Boat tail design of a missile is a big issue concerning the reduction of drag of the missile. Drag changes are estimated as a function of S_r , $S_r=S_{base}/S_{nozzle}$. Figure 3 shows Mach contours around the missile base with boat tail angle 16 degree with $S_r=1.45$. The jet-off simulation result is compared on the upper half and the jet-on simulation result is plotted on the lower half as shown in the Fig. 3. In case of jet-off, recirculation zone is appeared near the base accompanied by the shear layer adjacent to this recirculation zone. A Mach disk at about $0.3D$ distance from the base can be seen in the jet-on case because this flow is under expanded.

The jet-off base drag (blue dashed line with open rectangle symbol) goes up and the jet-off boat tail drag (blue dashed dot line with open rectangle symbol) goes down with the increase of S_r as shown in Fig.4. The jet-on drag thus steadily increases when the area ratio is increased. Both the base drag and boat tail drag when jet is on increase until the area ratio reaches 1.0.

Unsteady turbulent numerical simulation is done using some spike configurations in front of missile nose in an effort to reduce the drag. Pressure distributions and stream lines are shown in Fig. 5. Total drag reduction of 30 percent at low angle of attack is gained due to the break-up of bow shock from the spike. The calculated pressure oscillation is estimated at the frequency range of 800-1000Hz. The pressure oscillation frequency is measured from the flight test with the range of 900-1000Hz.

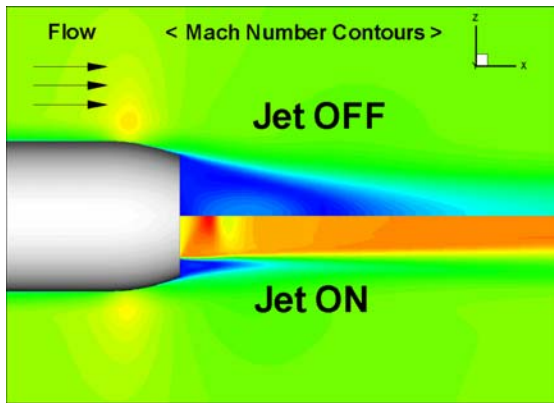


Figure 3. Mach contours with jet on/off, $Sr=1.45$, $M=0.85$, boat tail angle=16 deg.

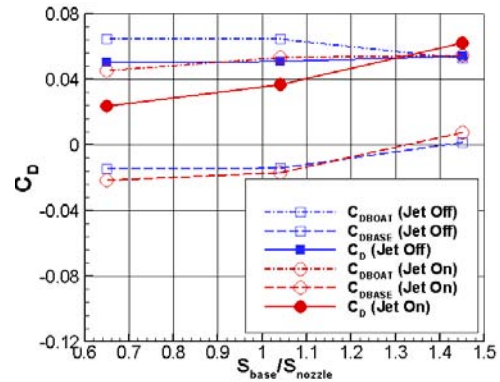


Figure 4. Drag curves for varied Sr , $M=0.85$, boat tail angle=16 deg.

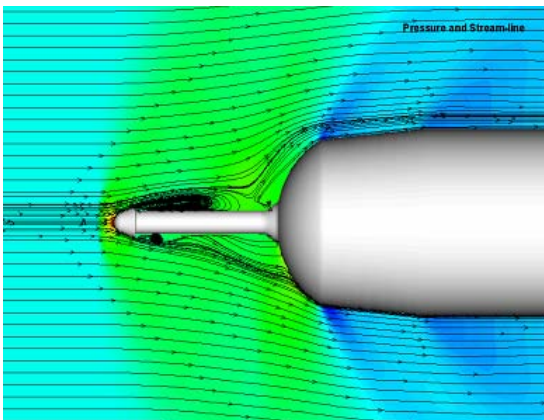


Figure 5. Unsteady turbulent flow analysis at $M=1.2$.

3.3 VLS Internal Flow Simulation with supersonic jet impingement onto wall

The VLS design challenge is to contain the initial impact of the jet plume and safely discharge the rocket exhaust gas during launch of the missiles. The challenge needs innovative mechanical design and extensive use of thermal protection materials that require understanding of the flow structures of the exhaust plumes. When the jet plume exhausts from rocket motor, the jet flow impinges on the bottom wall and then exits through the uptake after circulating in the plenum chamber.

To study the supersonic jet impingement inside the VLS plenum, flat plate jet impingement test case is simulated and validated experimentally at first. The computational geometry used for jet impingement onto flat plate is shown in Fig. 6. The nozzle is mounted perpendicular to the flat plate. The computational domain starts from the nozzle throat with Mach 1.0 condition. The boundary conditions of this nozzle throat are calculated from isentropic relations and perfect gas law. Strong normal shock is formed over the plate when a supersonic jet plume exhausts against the plate. If the grid system used in numerical computation is aligned with this normal shock, the shock instability occurs. Figure 7(a) shows Mach number contours in symmetric plane contaminated with shock instability, so-called “carbuncle problem”. This shock instability is cured by fixing near zero eigenvalue in the numerical dissipation term, yielding the stable results as shown in Fig. 7(b).

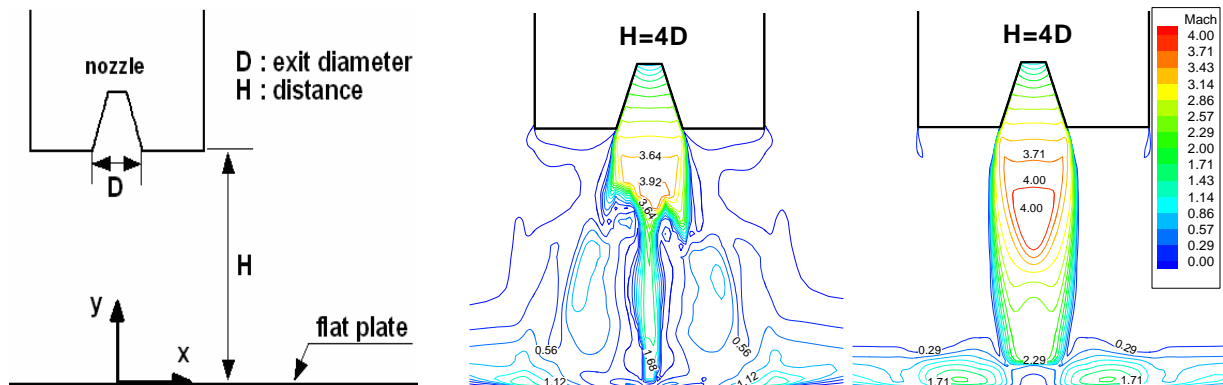


Figure 6. Computational model.

(a) without eigenvalue fixing (b) with modified eigenvalue
 Figure 7. Mach contours in symmetric plane for $H=4D$.

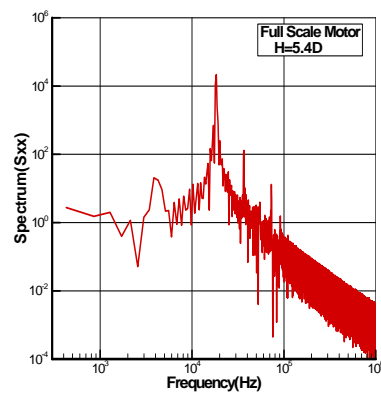


Figure 8. Spectra for $H=5.4D$.

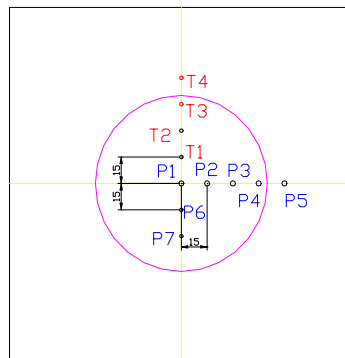


Figure 9. Sensor locations on the flat plate.

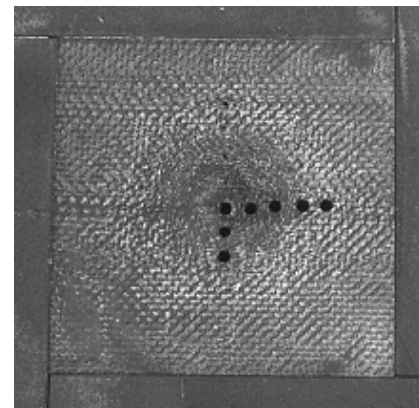


Figure 10. Ablation of flat plate after motor test.

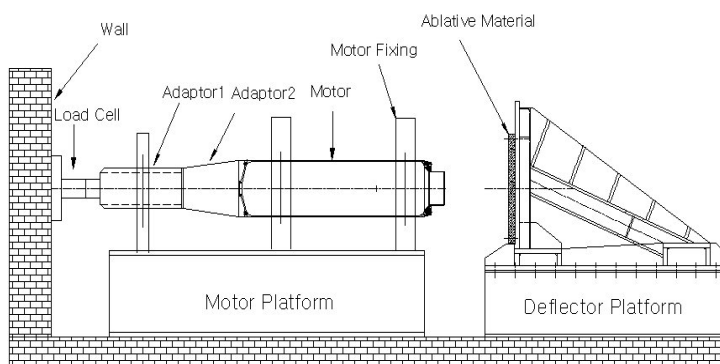
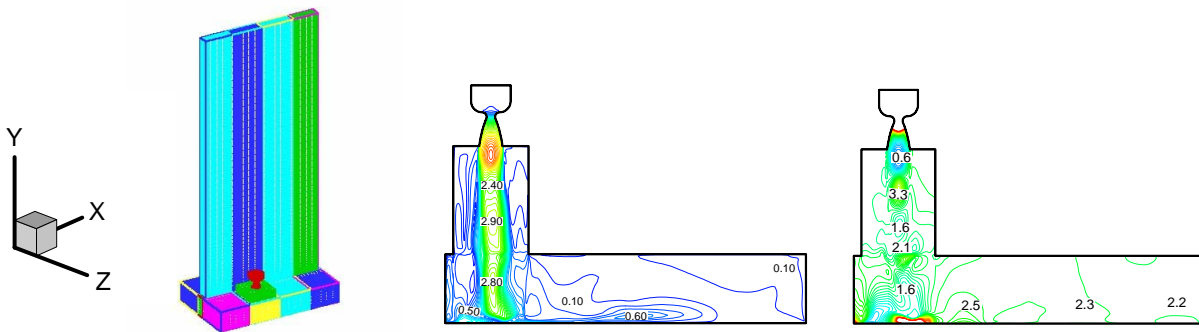


Figure 11. Sketch of motor test facilities (left) and actual test scene (right).

It is observed that the pressure oscillates with certain frequency. The pressure fluctuation at the center position reveals dominant frequency of 2.8kHz through the Fourier transform procedure as shown in Fig. 8. Pressure and temperature sensors are located on the flat plate with 15 mm space interval as shown Fig. 9 with seven pressure holes and four temperature gages. Figure 10 reveals the magnitude of ablation on the flat plate after the motor test. Figure 11 illustrates the test motor and the test setup.

The proven methodology on the supersonic jet impingement flow is then applied to VLS launcher. The computational grid system for flow simulation of VLS with 18 blocks are overlapped with neighboring blocks as shown Fig. 12(a). Flow simulations of only two motor cases are sufficient because of geometric similarity even though total of eight missiles are housed in VLS. Figures 12.(b) and 12.(c) show Mach contours and pressure contours of yz-plane view and xy-plane view, respectively, in the plane cutting through the motor.



(a) Overall grid (b) Mach contours in yz-plane (c) Pressure contours in yz-plane
Figure 12. Computational grid topology and Mach contours for VLS analysis.

Figure 13 shows the pressure distributions on the plenum bottom with 0.5 atm. interval. The maximum pressure is about 20 atm. as illustrated in Fig. 13. Since the primary interest is whether the jet plume is exhausted without causing too much erosion on the bottom as well as on the side wall, actual test firing was performed to partially verify the flow pattern as well as the ablation thickness. Pressure measure points at the plenum top plate are denoted in Fig. 14. The measured data and simulated results are compared in Fig. 15 and Fig. 16. The measured peak pressure at P1 which is at the nearest position to the motor in Fig. 15 is greater than the simulated pressure. The pressure at P5 shows good match between experimental and CFD data.

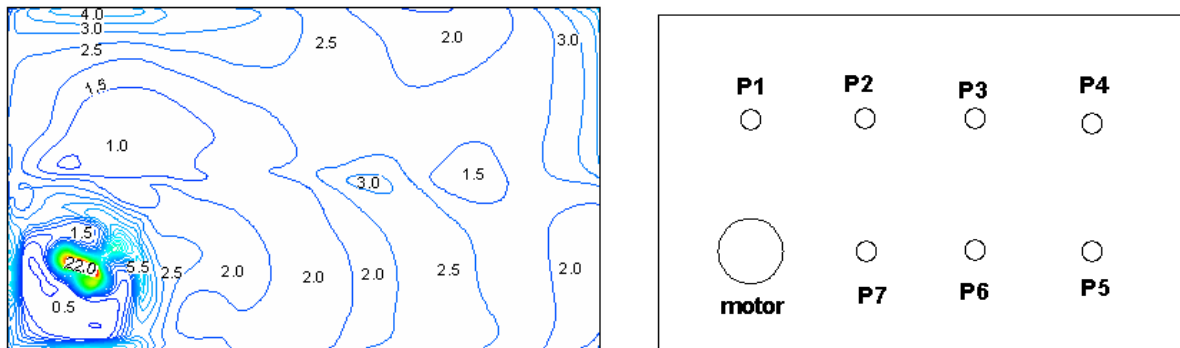


Figure 13. Pressure contours of plenum bottom wall with $\Delta P = 0.5$ (atm.).

Figure 14. Sensor locations on the plenum top plate.

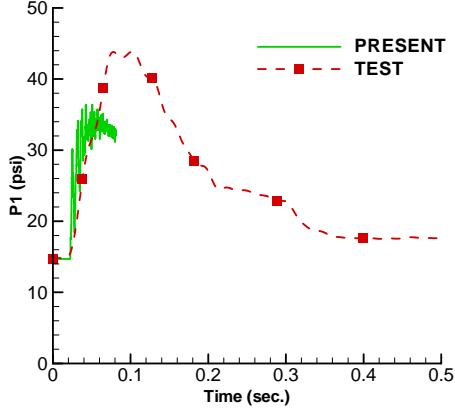


Figure 15. Pressure P1 comparisons.

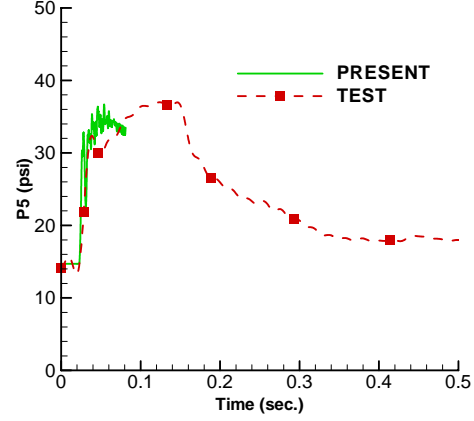


Figure 16. Pressure P5 comparisons.

3.4 Aerodynamic Modeling of Side Jet Influence on Body-Tail Missile Configuration

Side Jets are located on the forebody section to cause sudden changes in flight path. The location on the missile body is shown and a typical jet interaction flow pattern is summarized in Fig. 17. Figure 17 contains Mach contours in the symmetry plane when the side jet is turned on, capturing a strong bow shock and barrel shock, among other features. Both the pressure contours on the body surface and the wall pressure distribution near the jet exit plane illustrate severe changes in the pressure field. The exit flow condition of the side jet thruster is obtained from a separate simulation and reveals a very severe pressure condition. The jet exit pressure is about 500psi and exit Mach number, 2.4. The pressure ratio of the exit pressure to upstream pressure is, for example, 137 at 10km altitude. This ratio will increase as the flight altitude goes up and eventually pose a difficulty in conducting wind tunnel test.

A key question prior to wind tunnel test was to uncover the similarity law for the side jet conditions between the flight and wind tunnel models. The similarity parameters are i) static pressure ratio, ii) momentum flux ratio between free stream and jet exit plane, and iii) temperature ratio. However, the single most important similarity parameter may be the ratio between the upstream pressure and pressure at the jet exit plane. Primary aim of current side jet analysis is to provide 6DOF aerodynamic module for guidance and control simulation with and without side jet. However, the influence is likely a function of flight Mach number, altitude, angle of attack, orientation of jet, tail deflection and the number of side jets operated at one time.

After further CFD simulations and comparisons of data with data obtained from in-house wind tunnel tests, empirical formula which accounts for the effect of side jet force are defined as:

$$C_N = C_{N_{Without Jet}} + k_{C_N} N_{Jet} \frac{T_{Single Jet}}{Q_{ref} S_{ref}} \quad (5)$$

$$C_M = C_{M_{Without Jet}} + k_{C_M} N_{Jet} \frac{T_{Single Jet}}{Q_{ref} S_{ref}} \frac{L_{Jet}}{L_{ref}} \quad (6)$$

where,

$$k_{C_N} = f(\alpha, Mach, H, N_{Jet}, \phi_{Jet}) \quad (7)$$

$$k_{C_M} = g(\alpha, Mach, H, N_{Jet}, \phi_{Jet}) \quad (8)$$

where the empirical factor K was introduced for force and moment coefficients. It is called hereafter the jet effectiveness factor, K. This study thus explores the effect of side jet on pressure changes on the body-tail configuration or aerodynamic coefficients through the changes of this value from 1.0. The aerodynamic changes influenced by side jet activation can thus be quantified through the K factor for all components of forces and moments. If there is no side jet influence on the wall pressure changes on the body and tail. If it is greater or less than 1.0, that difference represents the amount of influence by the side jet.

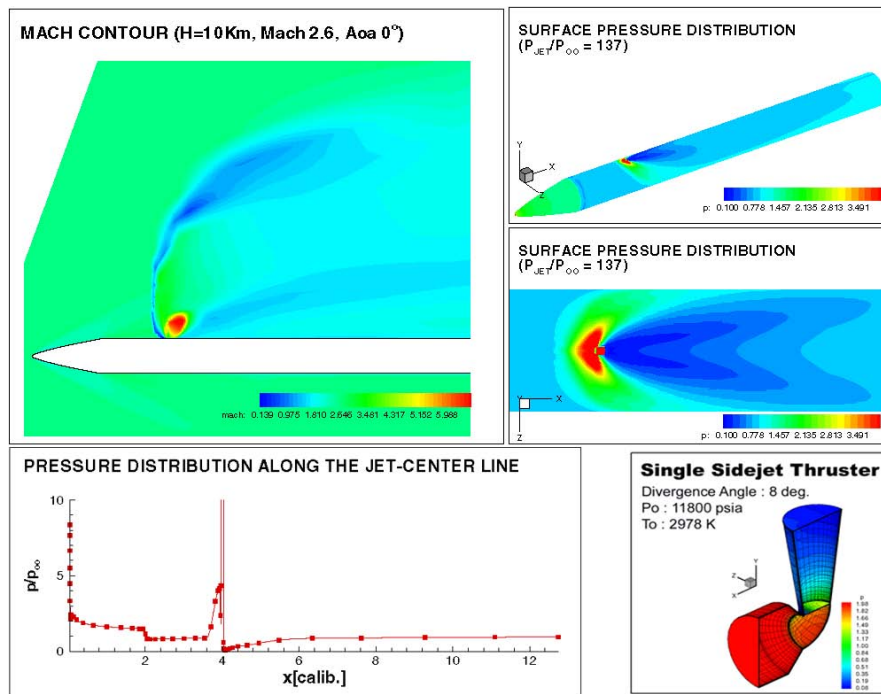


Figure 17. Jet interaction flowfield near and on the body surface.

Having studied the behavior of the jet effectiveness factor K computationally, wind tunnel test is still performed to map out the overall trend of the K factor for all flow and geometry parameters since the CFD alone can not cover the whole flight envelop. After much planning and preparation, two sets of wind tunnel tests have been conducted at the S2 and S3 wind tunnel facilities of ONERA at Modane in France March 2003 and April 2007. A test matrix was made to cover Mach, altitude, angle of attack, jet orientation or bank angle, and number of jets. Figure 18 shows a schlieren picture of flow field at Mach 2.3, pressure ratio of 150 with the jet on the leeward side. It shows nose shock, strong bow shock, barrel shock, expansion wave at the nose junction and a rather large wake region.

Results obtained from S2 tunnel are reprocessed to extract the jet effectiveness factor K. The K curves are then grouped and plotted for various flow parameters. Each curve is plotted as a function of angle of attack.

In general, strong interaction between the jet and the body is observed when the jet is activated on the windward side (Bank=180). The wall pressure on the body downstream of the jet goes up since the body shock generated from the nose confines the flow within the shock layer and thereby keeping the flow attached. All the K curves with the

windward jets are monotonous and show no deviation from the $K=0$ for the K_y , implying there is no side force. This behavior is consistent for all the test cases.

On the other hand, weak interaction is observed when the jet is injected into the leeward side (Bank=0). At high angles of attack, the K_z curves show a sudden dip in the range of 14 to 18 degrees of AoA, for example, at Mach=2.3 and pressure ratio 150. A notable feature is that the K_y curves show deviation from $K_y=0$ at AoA greater than 7 deg. This means side force is generated even though the flow is supposed to be symmetric. This prompted close scrutiny as to what is happening for the leeward jet flow.

In Figs. 19 through 21, jet effectiveness factor for normal and side force components, K_z and K_y respectively, is displayed for Mach 2.3, PR 150, and leeward jet which is the same case shown in Fig. 6. As opposed to the windward jet, the leeward jet interacts with the body vortex when the angle of attack reaches a certain value. It is indeed observed from the schlieren pictures that the onset of body vortex travels upstream and interacts with the bow shock. When this happens, the bow and barrel shock suddenly become fuzzy and seem to vibrate, causing the flow asymmetrical. The amount of side force is not negligible and is as much as 20 percent of the normal force at low pressure ratio.



Figure 18. Schlieren graph at Mach 2.3 with leeward jet.

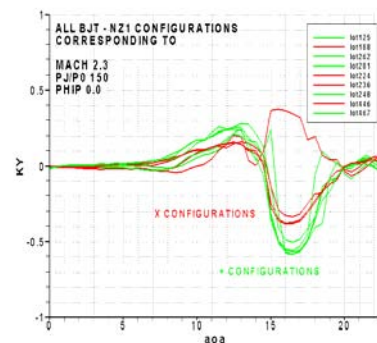


Figure 19. K_z as a function of AoA at $M=2.3$ with leeward jet.

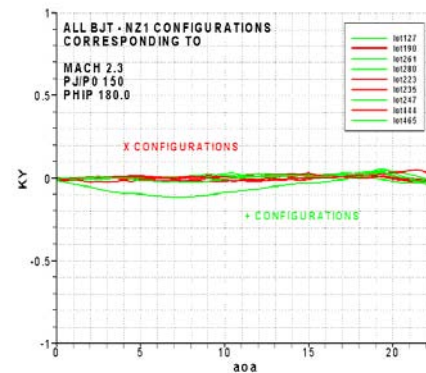
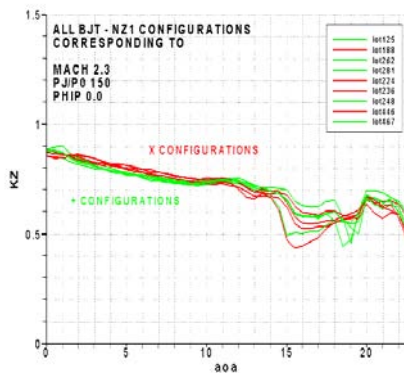


Figure 20. K_y as a function of AoA at $M=2.3$ with leeward jet.

Figure 21. K_y as a function of AoA at $M=2.3$ with leeward jet.

In Figs 22 and 23, side force factor, K_y , is displayed for varied Mach numbers. Fluctuations are measured at low Mach number with leeward jet as shown Fig. 22. This side jet wind tunnel tests show the complementary aspect of experiment. While CFD displays detailed flow behavior of transverse jet interactions, the seemingly random features of extra yaw at high angles of attack can only be ascertained by the testing. This shows still a restricted role of CFD in the course of missile aerodynamic design.

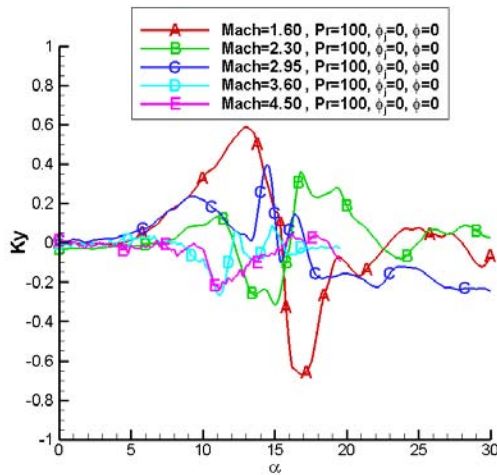


Figure 22. K_y as a function of AoA with leeward jet for varied Mach no.

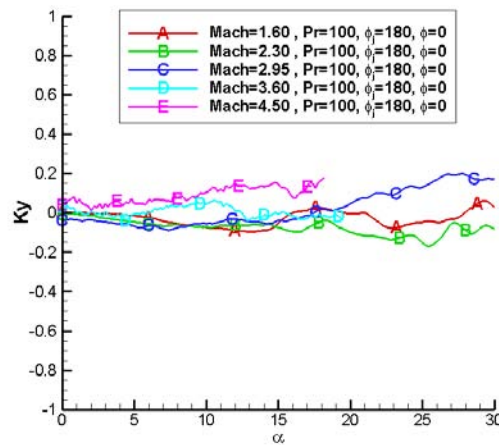


Figure 23. K_y as a function of AoA with windward jet for varied Mach no.

4. Conclusions

Four flow simulations mentioned here exemplifies the usefulness of CFD for illustration of flow behavior. The complex nature of shock/boundary interaction, transverse jet interaction and jet impingement are well captured numerically and their accuracy is validated through wind tunnel testing or a special set up. As was shown, the high angle of attack side jet flows were not well perceived prior to the wind tunnel test, exemplifying a need for computation and its validation.

Future activities at the ADD aero lab include multidisciplinary optimization in an effort to accelerating the design cycle.

References

- [1] Lee, K. S., Hong, S. K., and Park, S. O. Improvement in Flux-Difference Splitting Algorithm for Accurate and Robust Flow Simulation. *Computational Fluid Dynamics Journal*, Japan, Vol. 10, No. 2, July 2001.
- [2] Kwang-Seop Lee, Seung-Kyu Hong and Seung-O Park. Supersonic Jet Impingement Navier-Stokes Computations for Vertical Launching System Design Applications. *Journal of Spacecraft and Rockets*, Vol.41, No. 5, September-October 2004, pp.735-744.

- [3] R. P. Peklis. Surface Pressure Measurement on Slender Bodies at Angle of Attack in Supersonic Flow. Memorandum Report ARBRL-MR-02876, 1978.
- [4] D. Degani, L.B. Schiff and Y. Levy. Numerical Prediction of Subsonic Turbulent Flows over Slender Bodies at High Incidence. *AIAA Journal*, Vol. 29, No. 12, 1991.

CFD Applications and Validations in Aerodynamic Design and Analysis for Missiles

Kwang-Seop Lee and Seung-Kyu Hong
Agency for Defense Development

**3rd International Symposium on Integrating CFD
and Experiments in Aerodynamics**

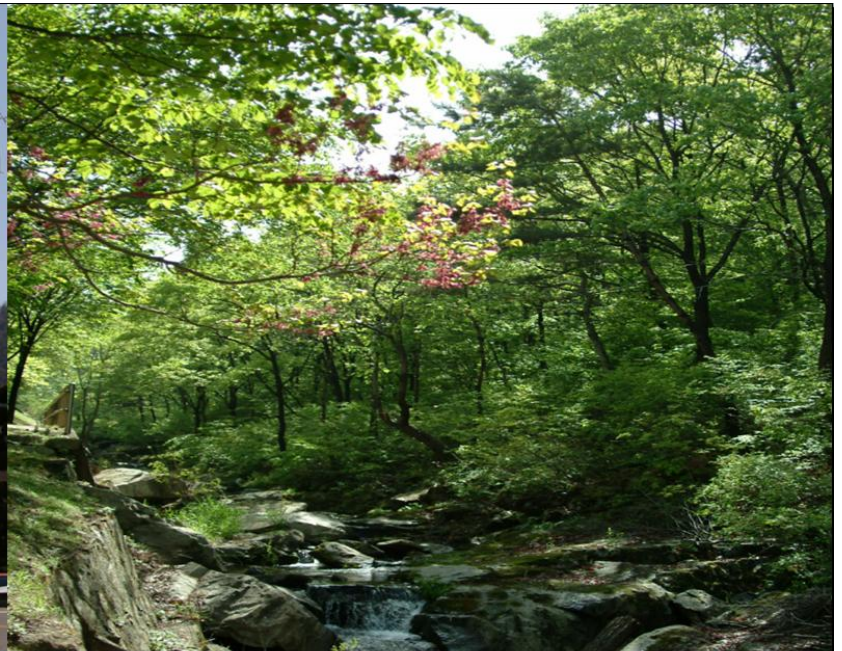
20-21 June 2007
USAF Academy



Outline of Talk

- **ADD Brief**
- **Numerical Method**
- **Applications**
 - **Ogive-cylinder**
 - **Boat tail and Spike**
 - **VLS Internal Flow**
 - **Side jet on body-tail missile**
- **Conclusions**







Military Demarcation Line



US Navy LOGIR Team Visits to ADD



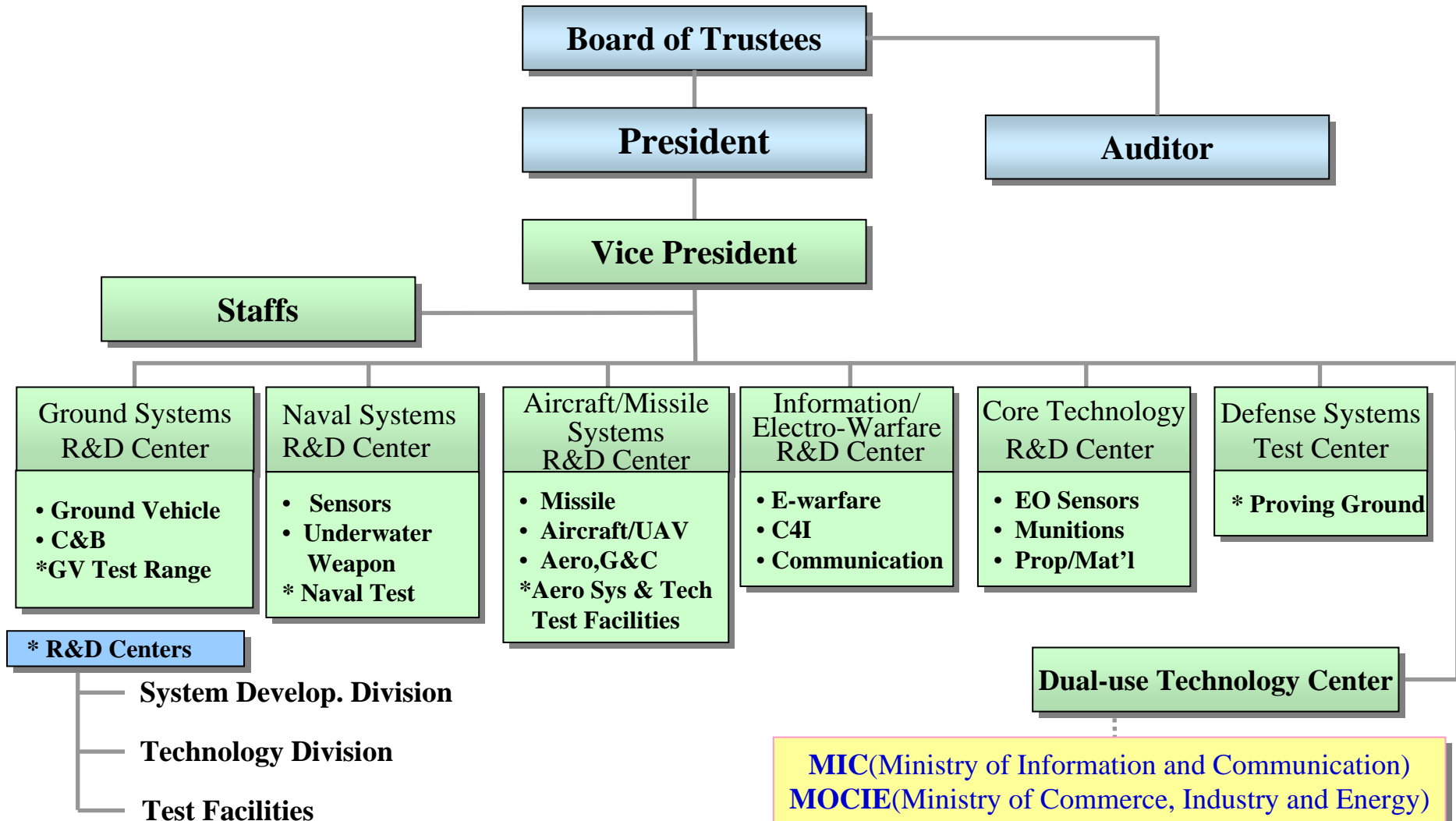
Cultural Exposure



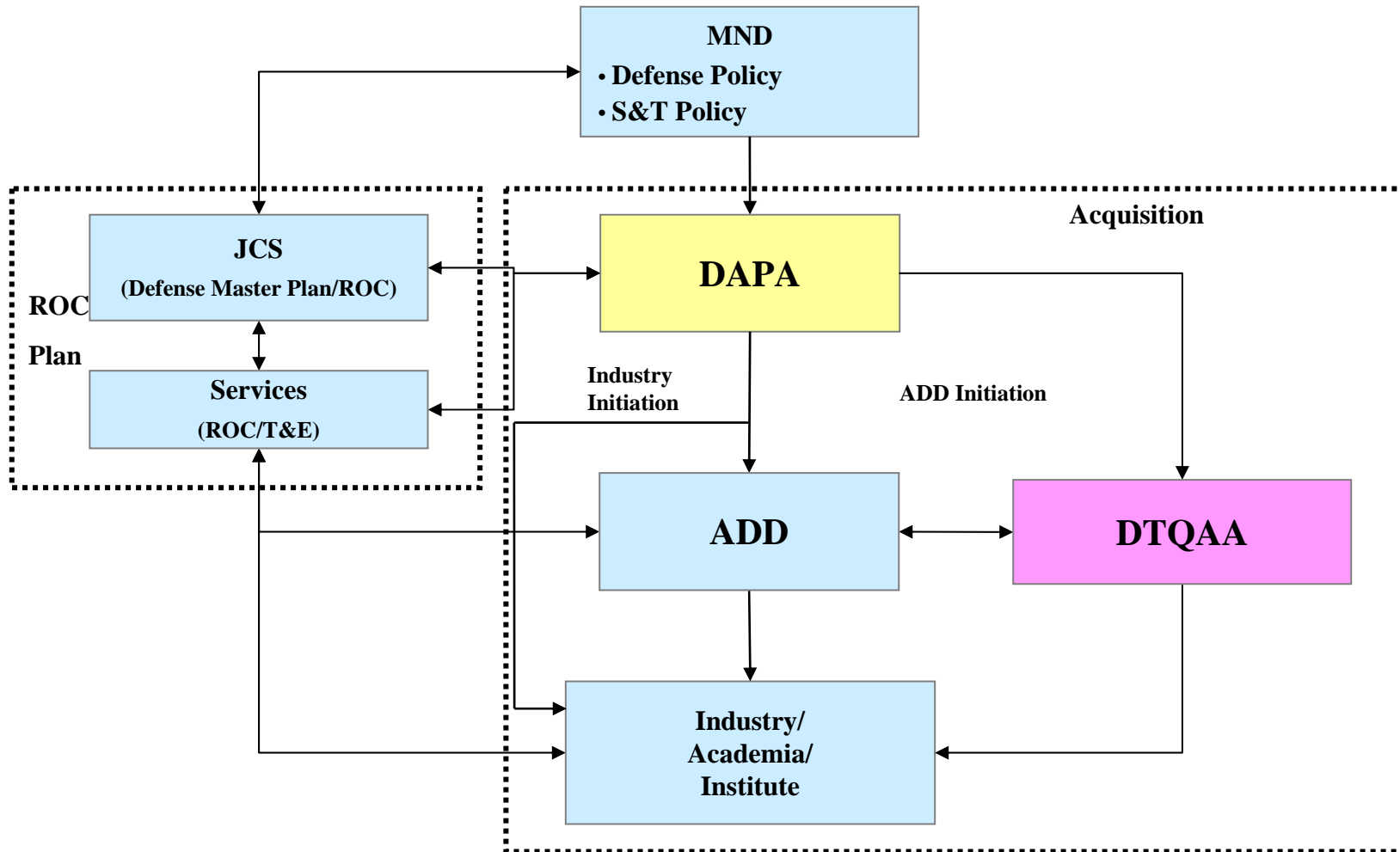
Cultural Exposure



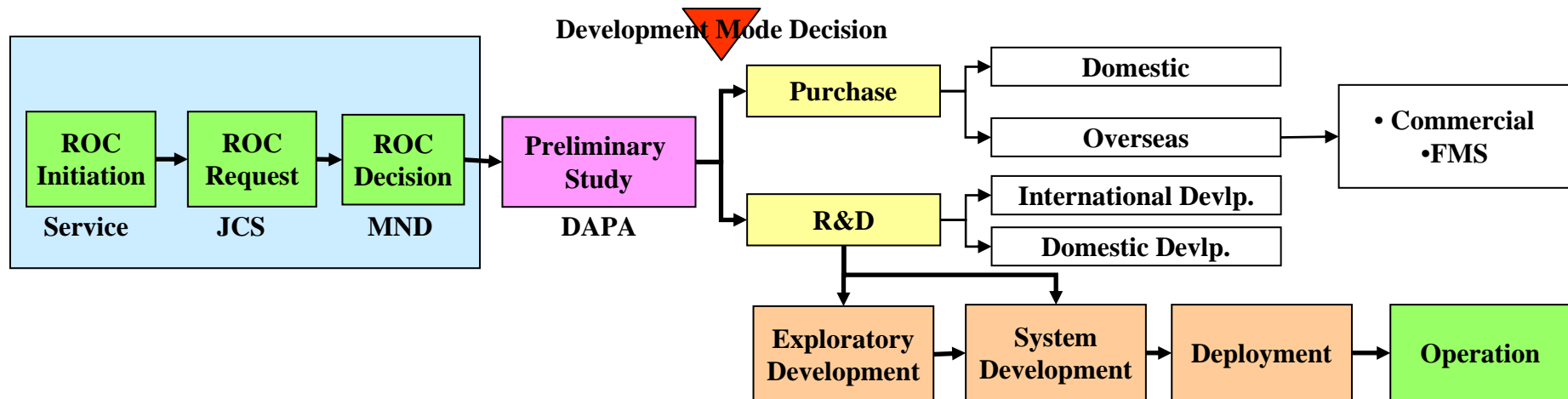
ADD Organization



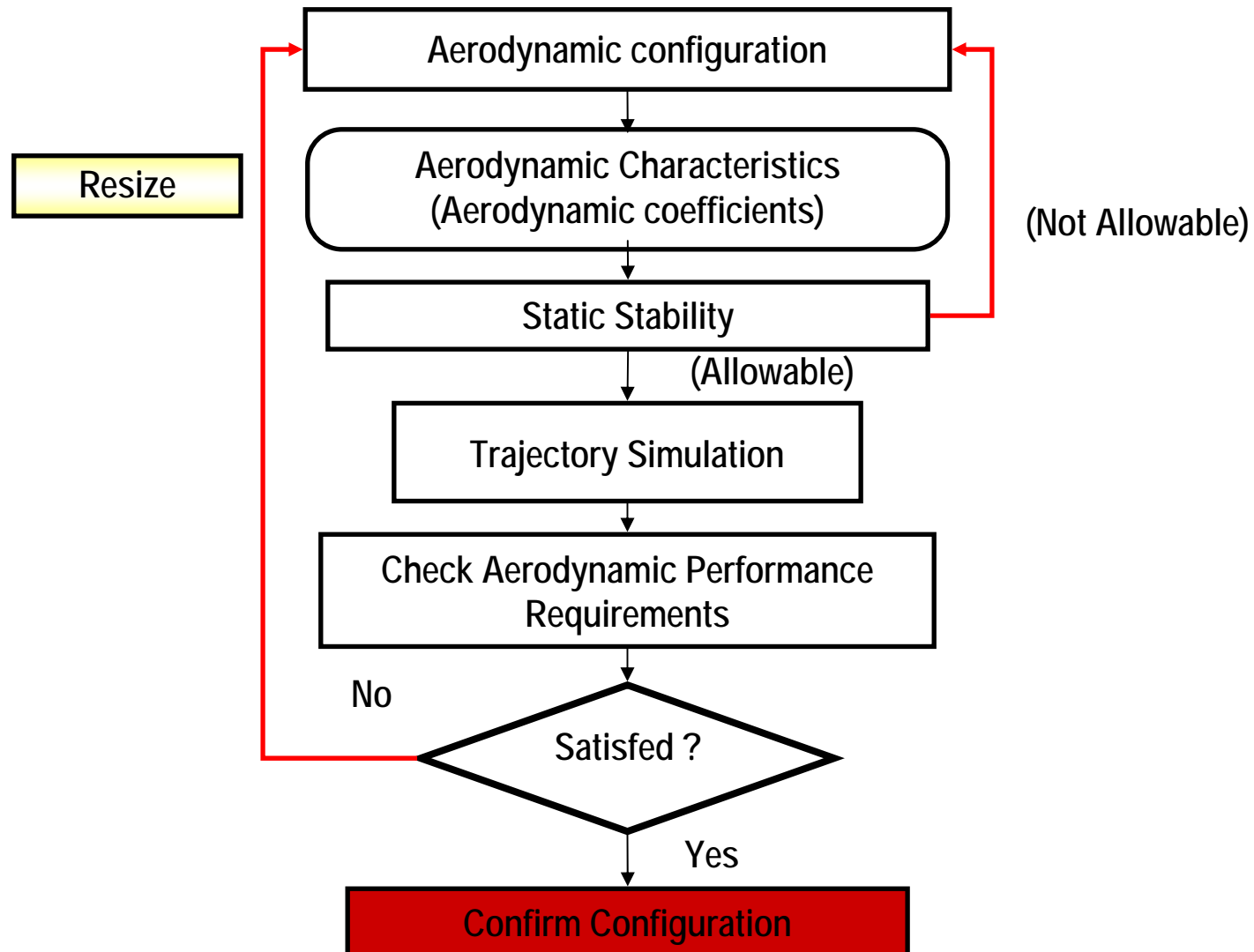
R&D and Acquisition Flow



System Development Flow



Procedure of Aerodynamic Design



Aerodynamic Analysis

- **Aerodynamic coefficients**
 - prediction code
 - W/T tests
 - 6DOF table (trajectory simulation, design of autopilot)
- **Aerodynamic load**
 - trim condition
 - panel code
 - CFD
 - structural test
- **Hinge moment**
 - determine hinge axis
 - hinge moment on hinge axis
 - W/T tests for hinge moment



Analysis Tools

- **Semi-empirical prediction tool**
 - for the static and dynamic aerodynamic coefficients
 - for hinge moment
 - for aerodynamic loads
- **Panel method aerodynamic prediction tool**
 - for aerodynamic coefficients
 - for aerodynamic loads
- **Computational Fluid Dynamic (CFD) aerodynamic prediction tool**
 - in-house code
 - commercial code



CFDS Numerical Method

- **Flux-Difference Splitting Method**
- **Finite Difference Method**
- **3-D Navier-Stokes Solver**
- **Multiple Blocks**
- **Characteristic Boundary Conditions**
- **Baldwin-Lomax Turbulence Model**
- **Two 1-Equation Models**



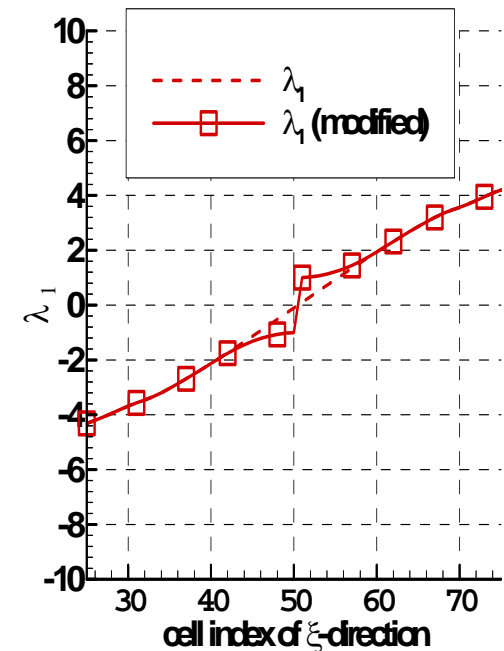
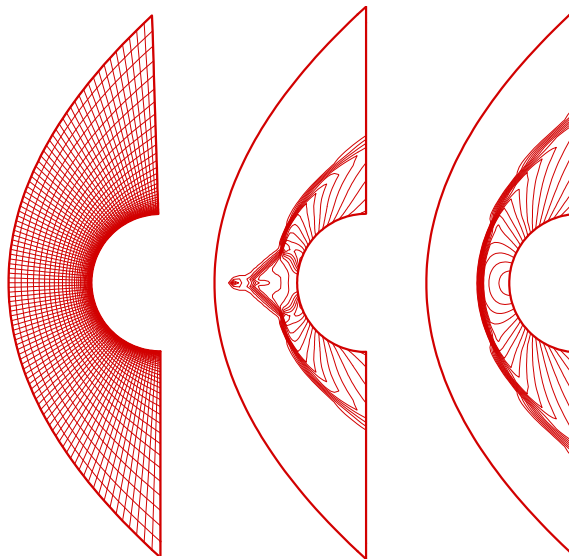
CFDS Shock Fixing

$$|\lambda| = \left(\frac{\lambda^2 + \varepsilon^2}{2\varepsilon} \right) \quad \text{if} \quad |\lambda| \leq \varepsilon$$

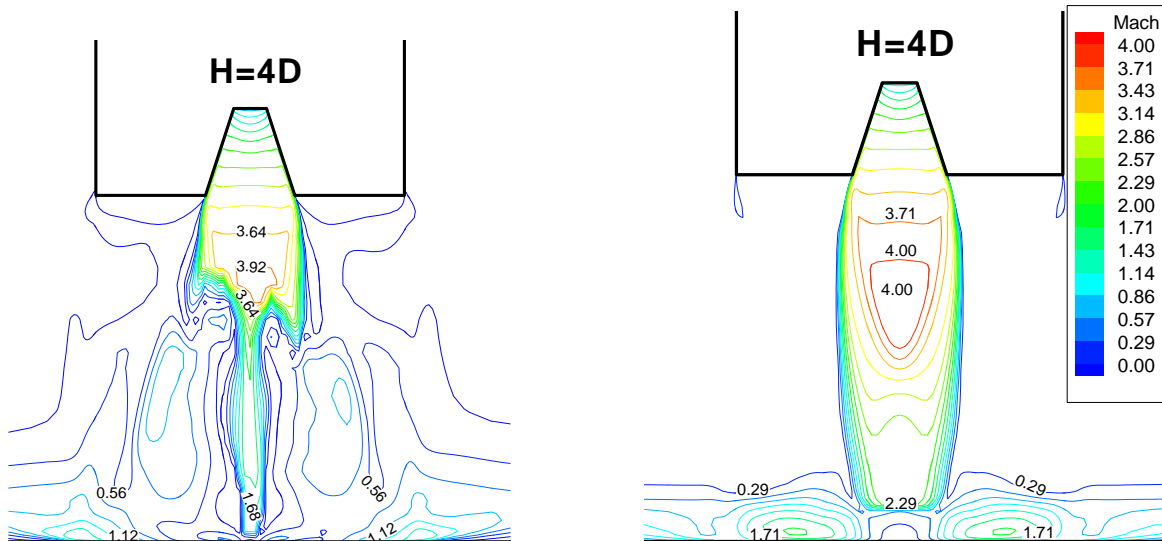
where, ε = constant

AIAA-95-1732-CP

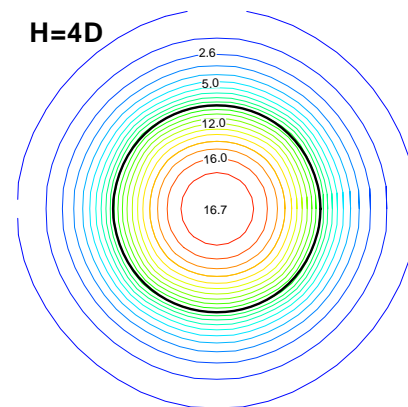
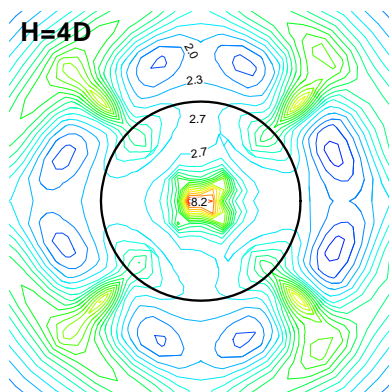
- **M=8.0**
- **AOA = 0.0 deg.**
- **Re=1.9x10E8**
- **Mesh 101x50**



CFDS Shock Fixing



**Shock
Instability**



**Instability
Cured**

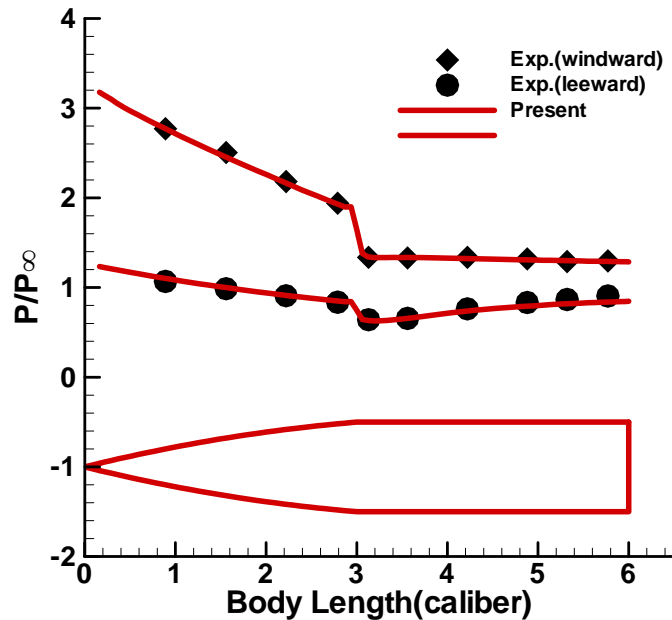


Supersonic Ogive-Cylinder

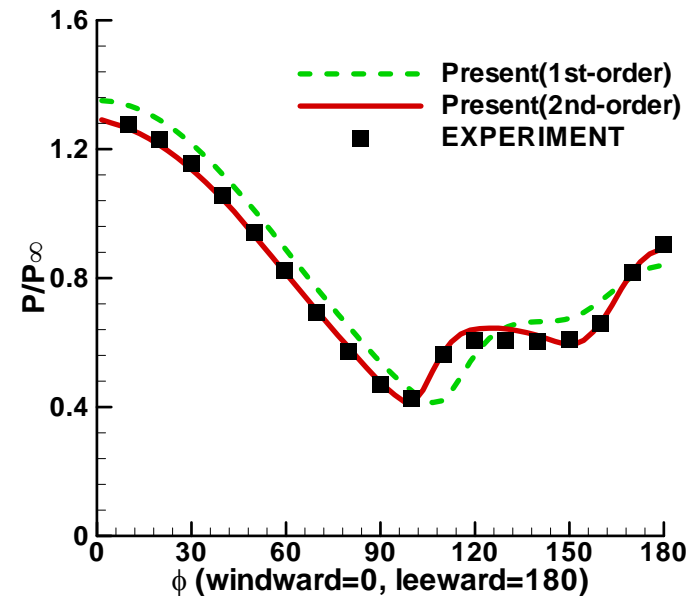
- **Mach=3.0**
- **AoA=10.0 deg.**
- **Re=6x10⁶**
- **Grid=84x65x62**
- **Baldwin-Lomax Turbulence Model**
- **Degani-Schiff Modification**



Supersonic Ogive-Cylinder



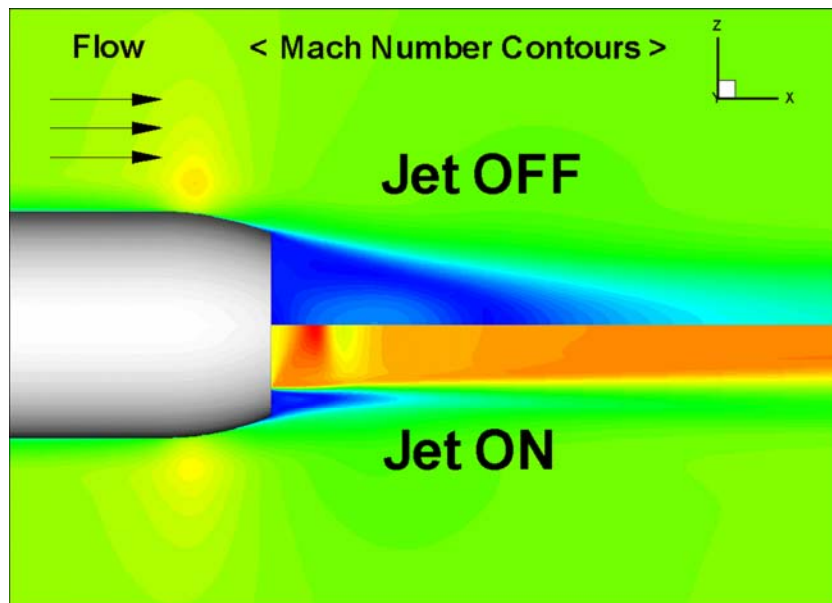
Surface pressure



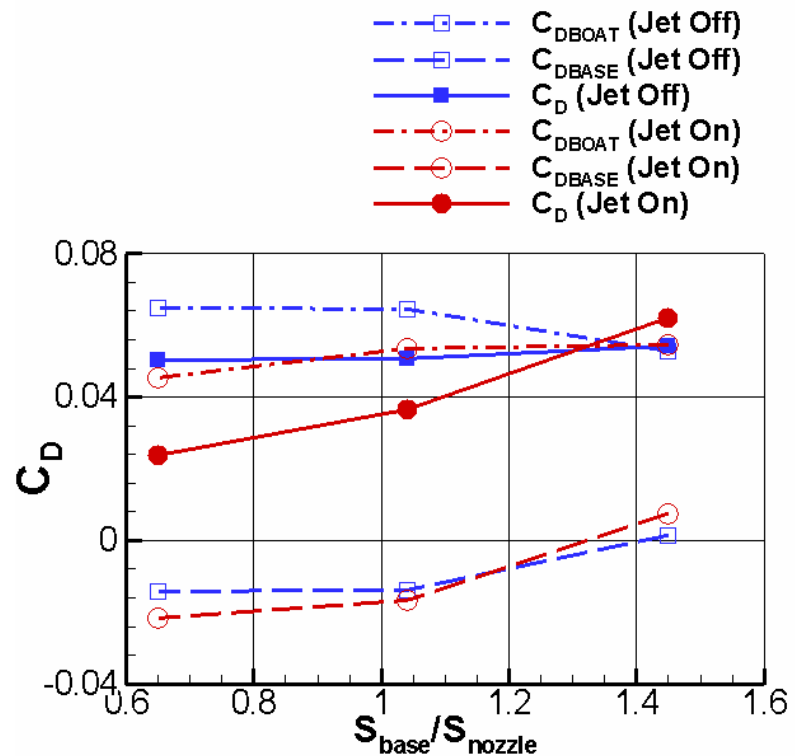
Circumference pressure



Boat-Tail Design



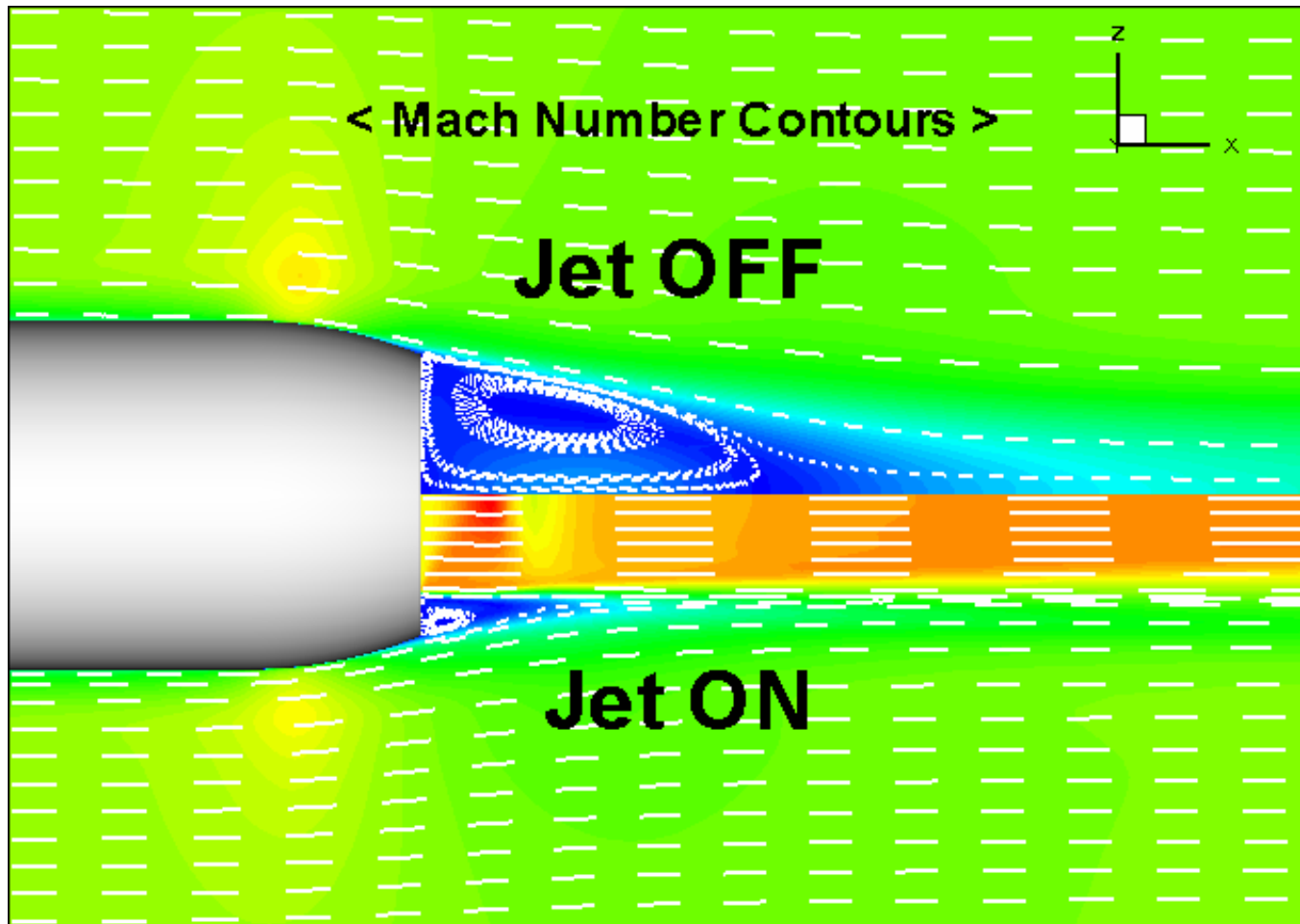
Mach contours, $Sr=1.45$, $M=0.85$



Drag curves

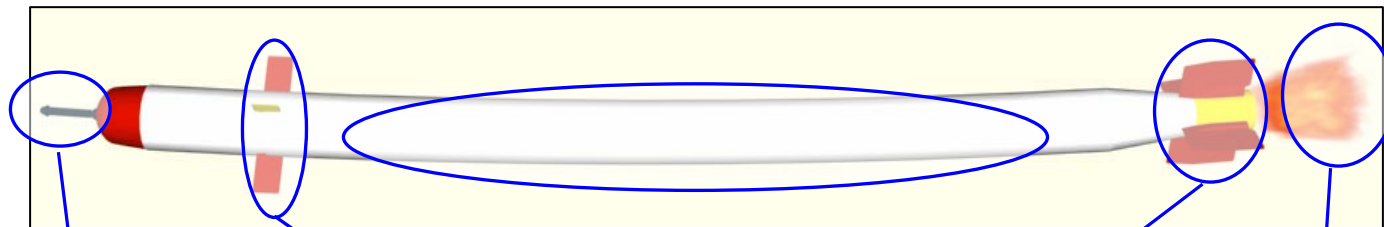


Boat-Tail Design

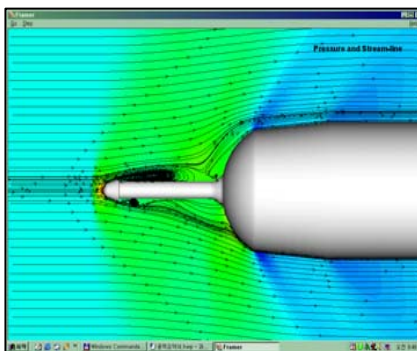


Mach contours, $Sr=1.45$, $M=0.85$

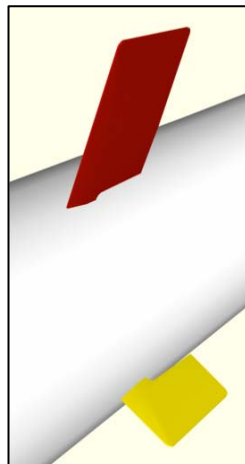
Aerodynamics for Man-Portable SAM



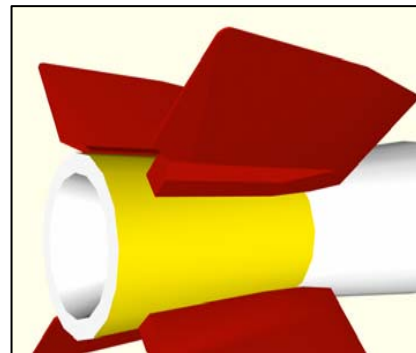
**Aerodynamic Analysis of
Flexible Body**



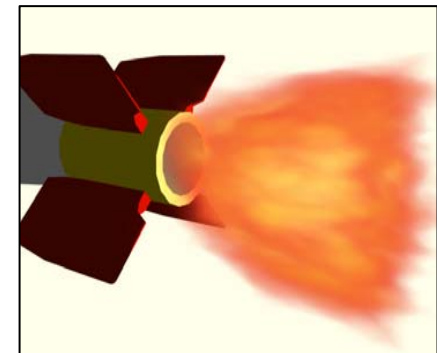
**Spike Flow Simulation
(Drag Reduction)**



Asymmetric Fin



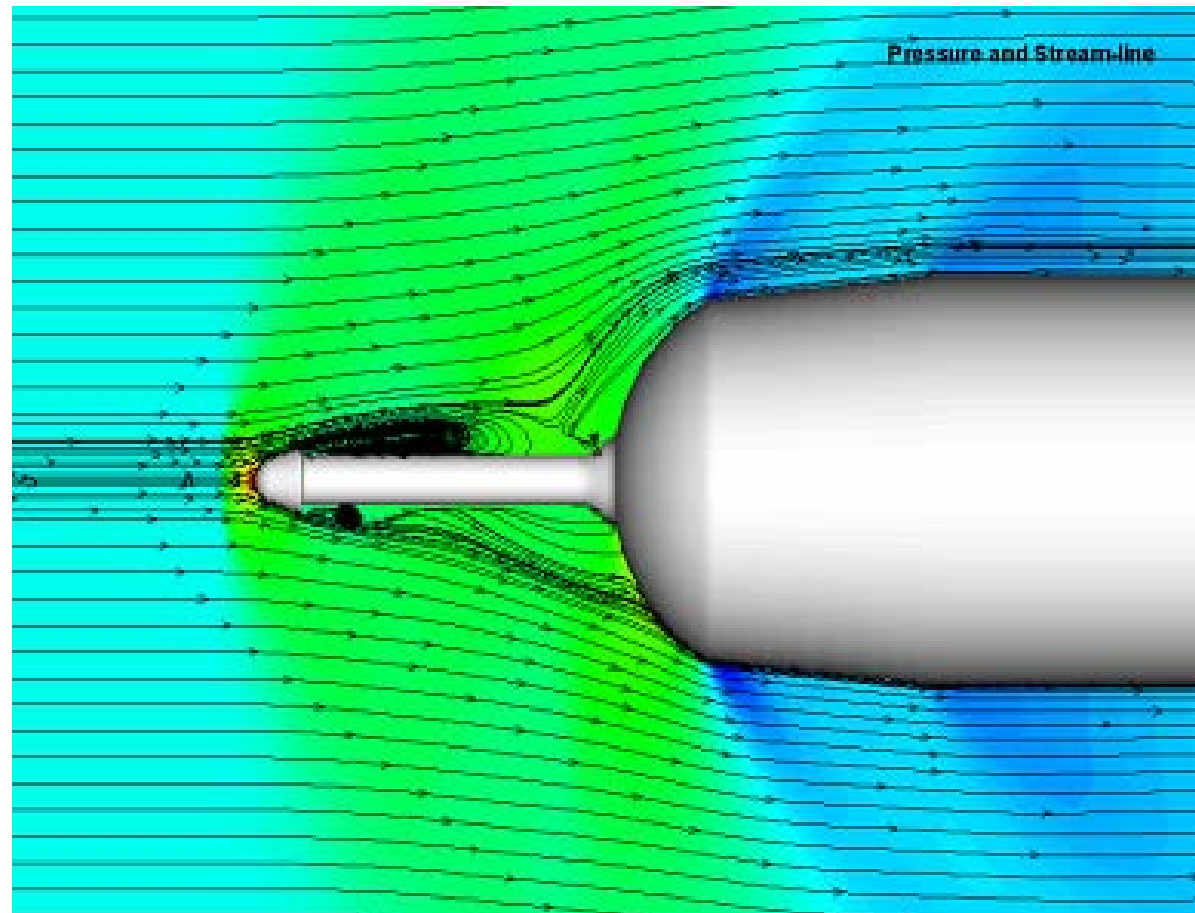
Roll Induced Device



**Aerodynamic Interference
with Thrust Plume**



Spike Design



Unsteady turbulent flow, $M=1.2$



Jet Impingement onto Flat Plate

Motor Characteristics

	Test Motor	Full-Scale
--	------------	------------

	Test Motor	Full-Scale
• Chamber Pressure	1200 psia	1750 psia
• Chamber Temperature	2950 K	2970K
• Thrust	330 lbs	1500 lbs
• Throat Diameter	12.0 mm	67.0 mm
• Exit Diameter	32.6 mm	182.6 mm
• PR	1.87	2.33
• Exit Mach	2.93	2.93

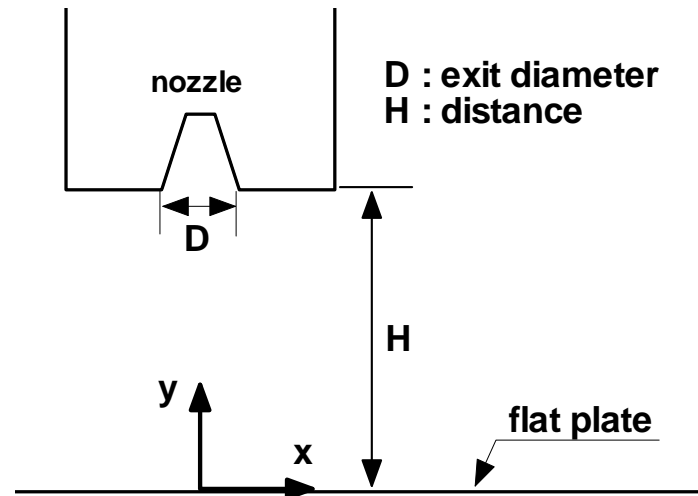


Jet Impingement Problems

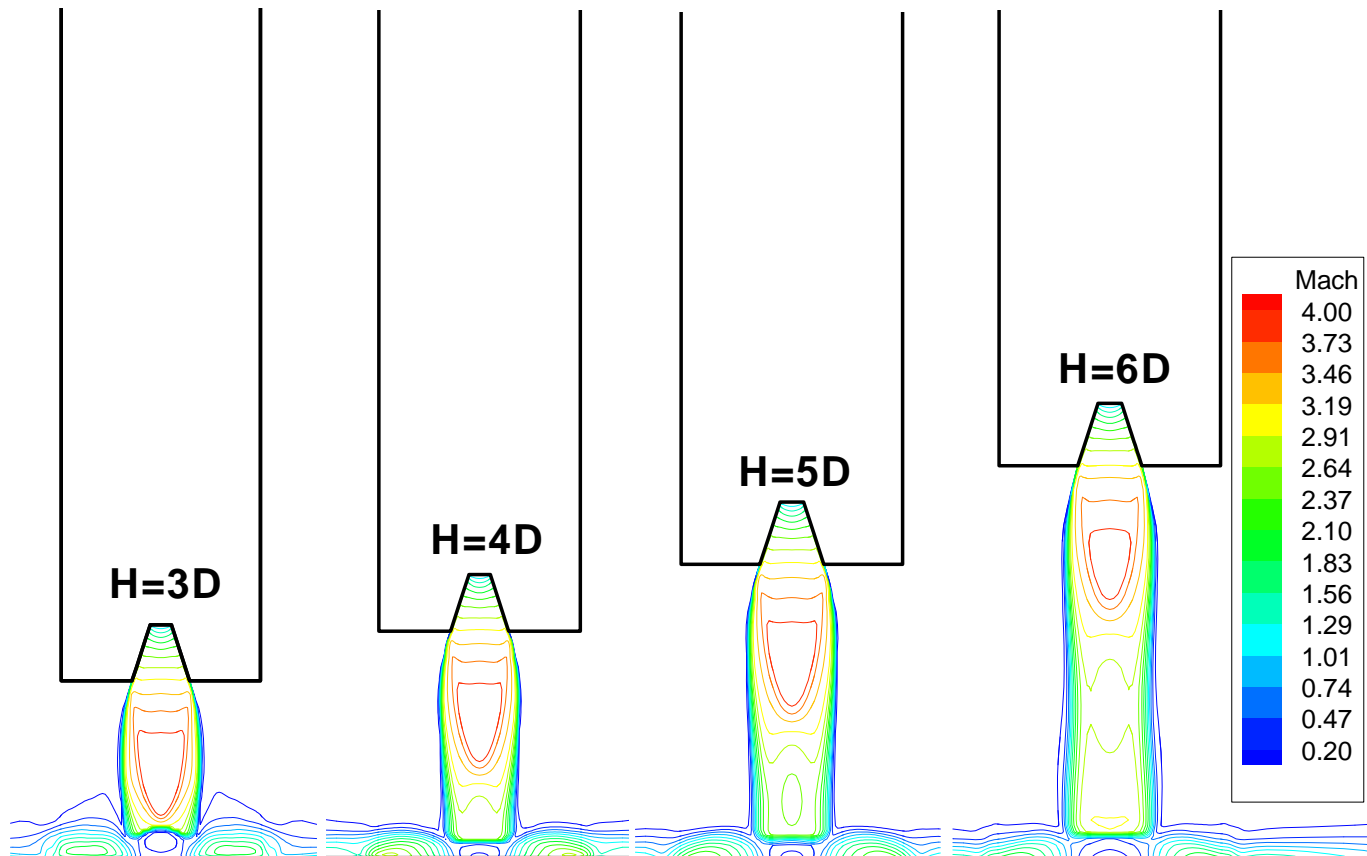
- Test Motor
 $H=3, 4, 5, 6D$
- Full-Scale Motor
 $H=5.4D, 7.6D$

Main Parameter

- PR (Pressure Ratio)
- Me (Exit Mach no.)
- H/D (Distance)



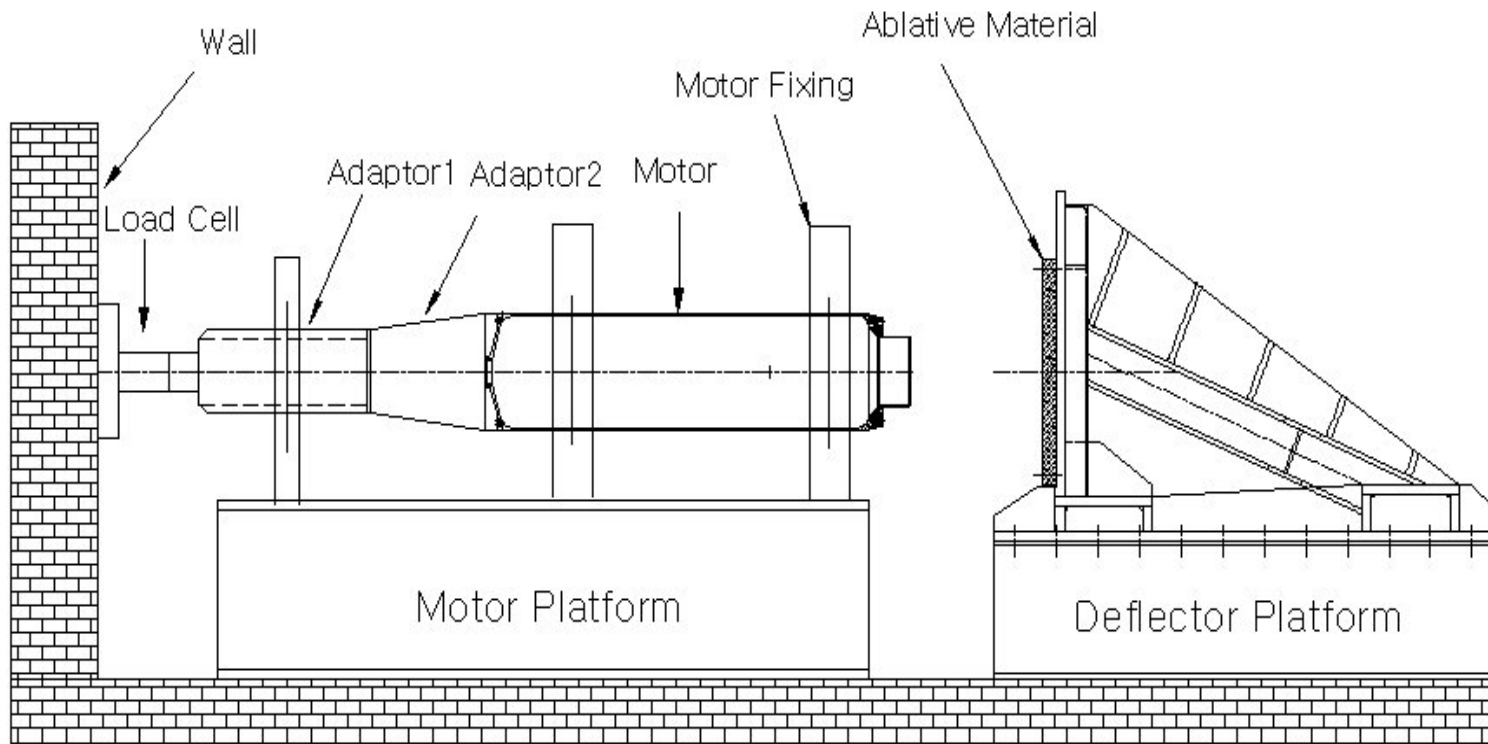
Test Motor Simulations



Mach Contours for Varied Distance



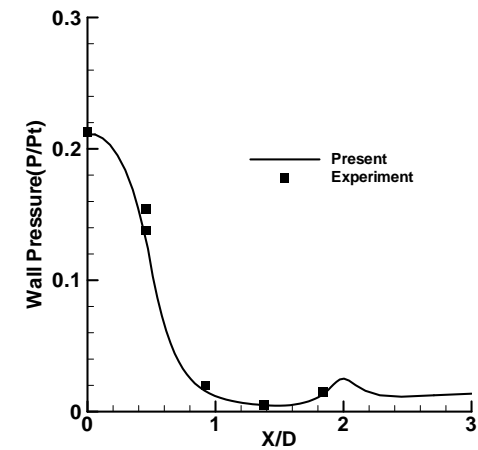
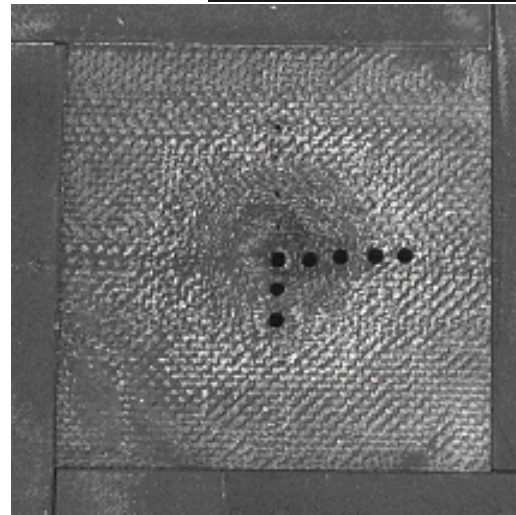
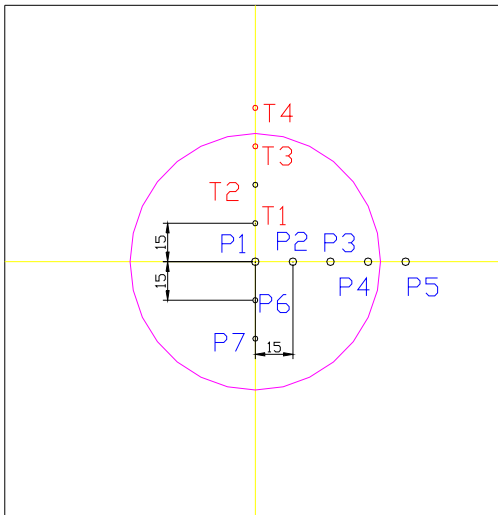
The Motor Test



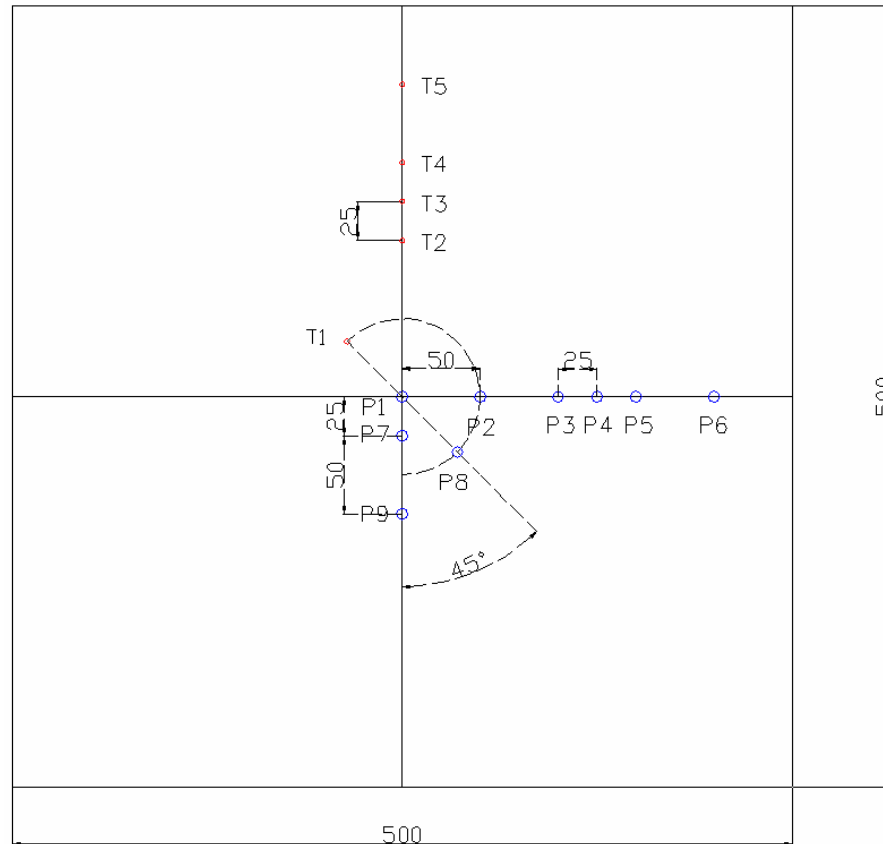
Experiment Facilities



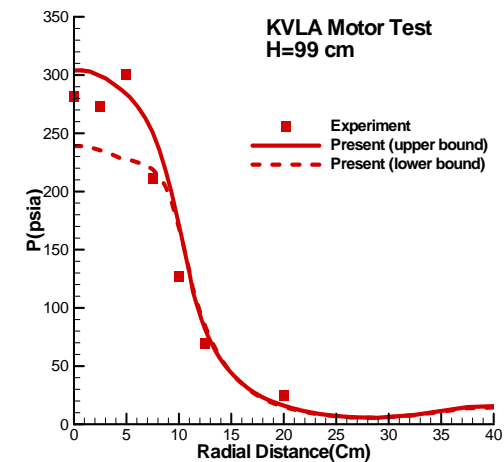
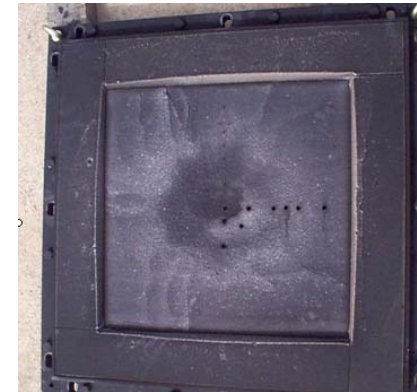
The Motor Test



Full-Scaled Motor Test



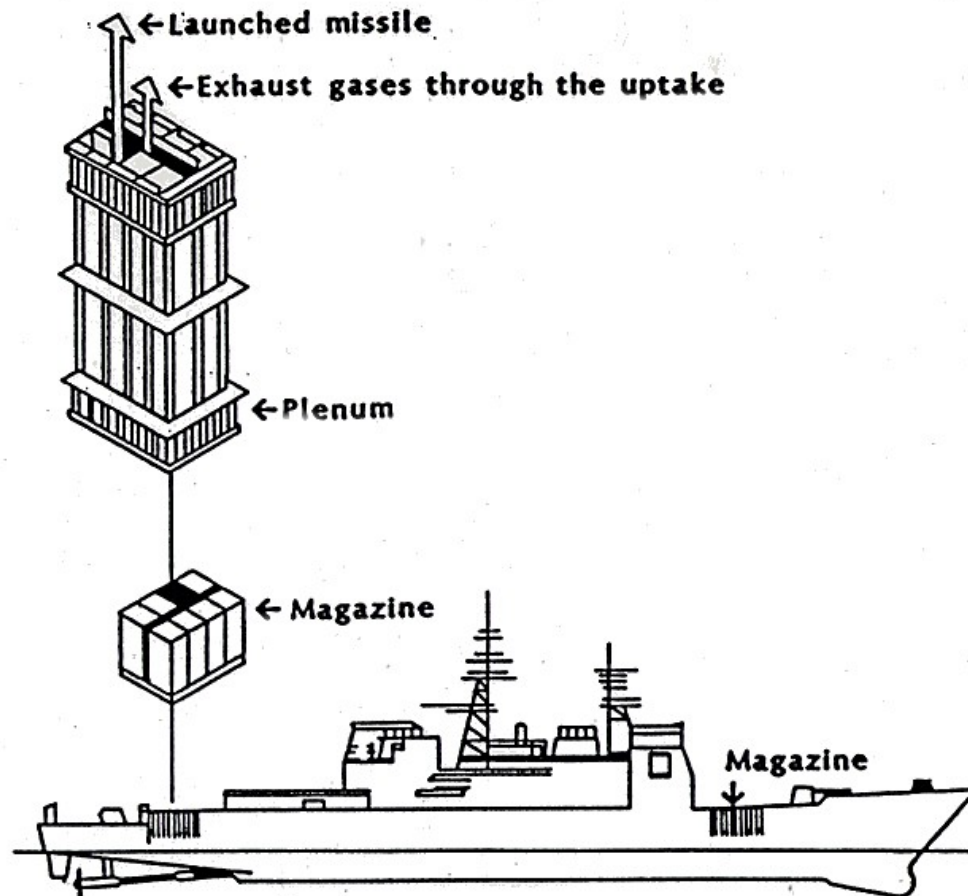
Pressure and Temperature Measure Locations



Pressure Distribution



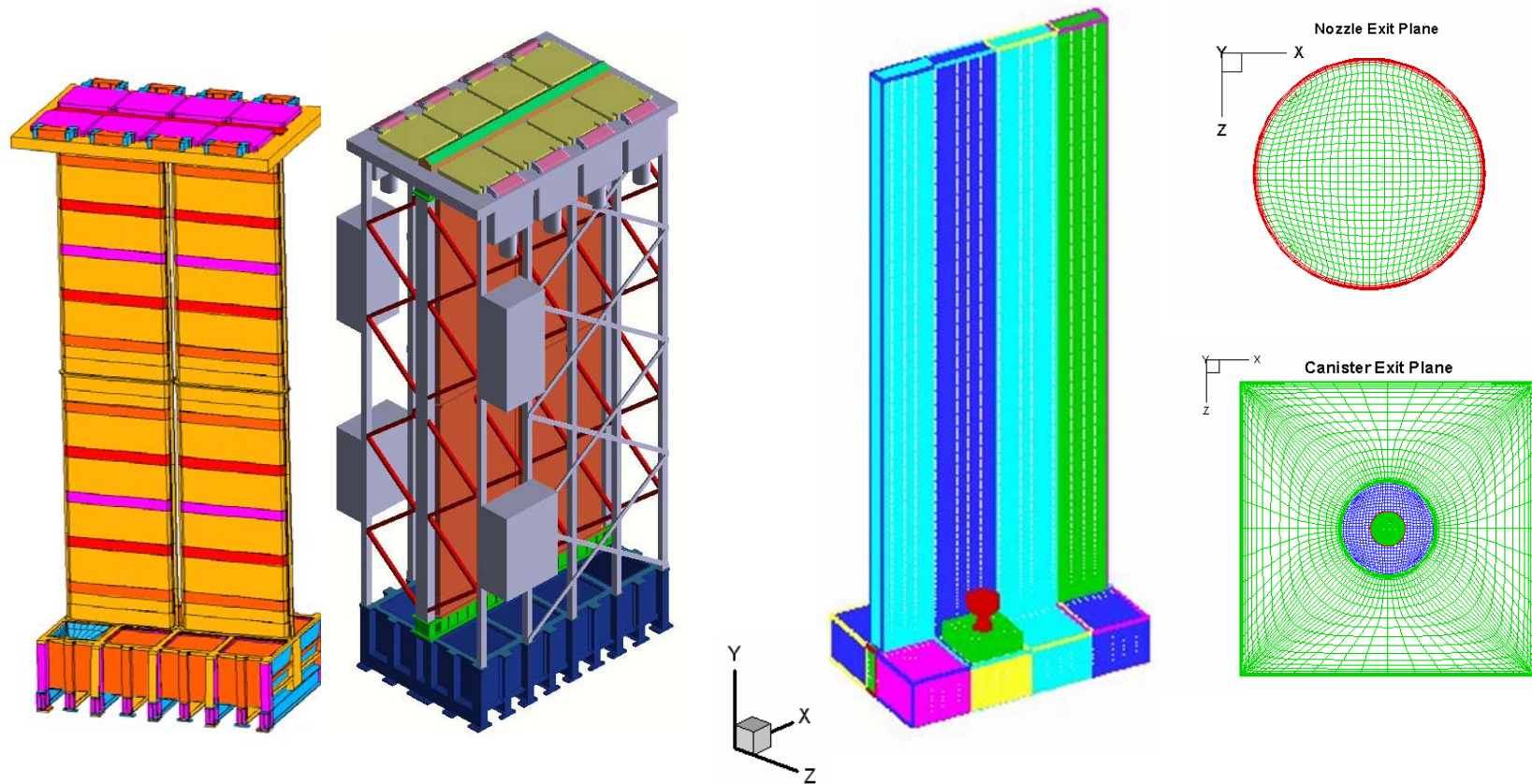
VLS Internal Flow Simulations



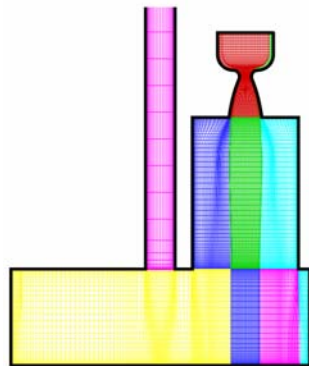
Sketch of a full scale Vertical Launching System (VLS)



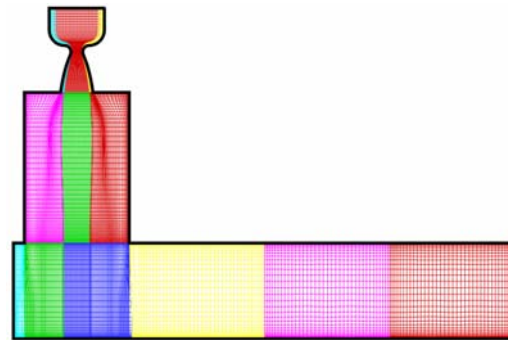
Grid systems



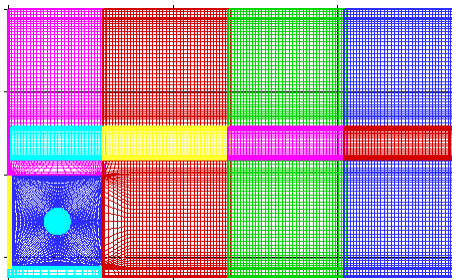
VLS Grid System



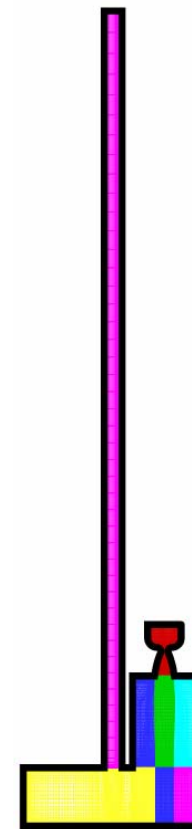
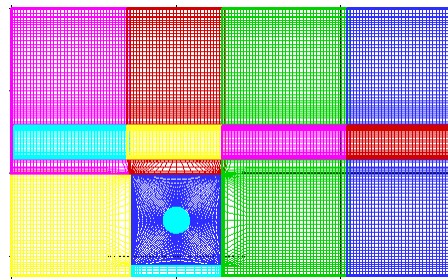
yz-plane



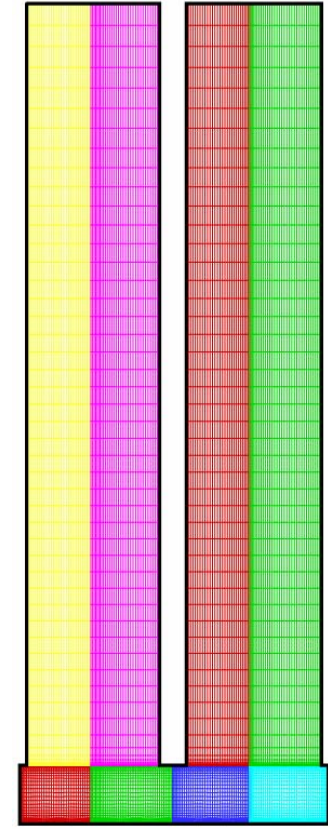
xy-plane



xz-plane



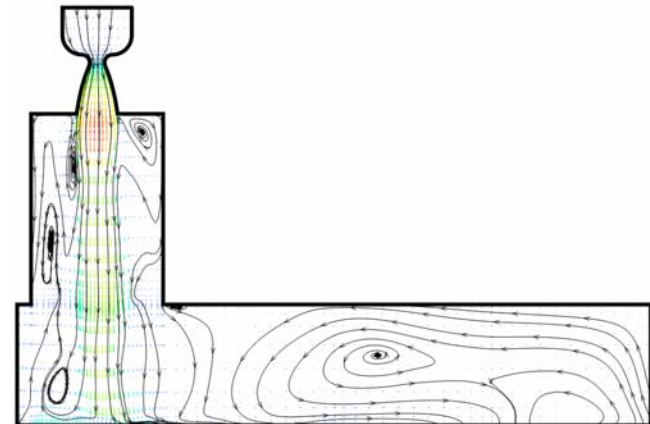
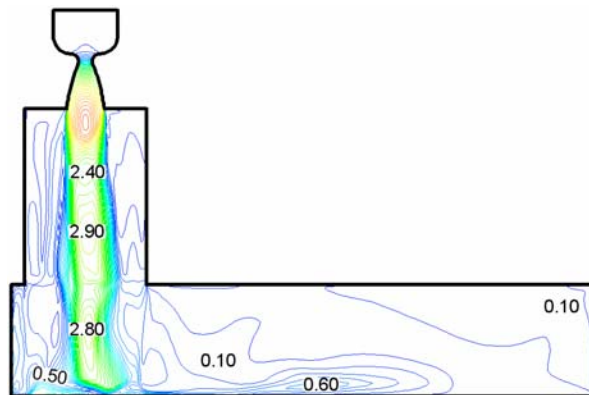
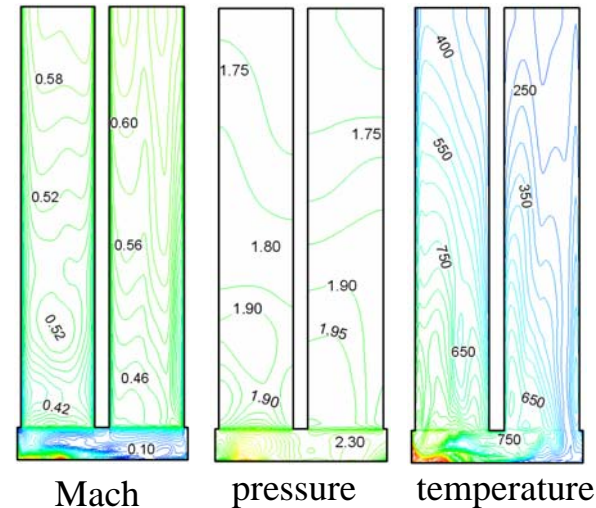
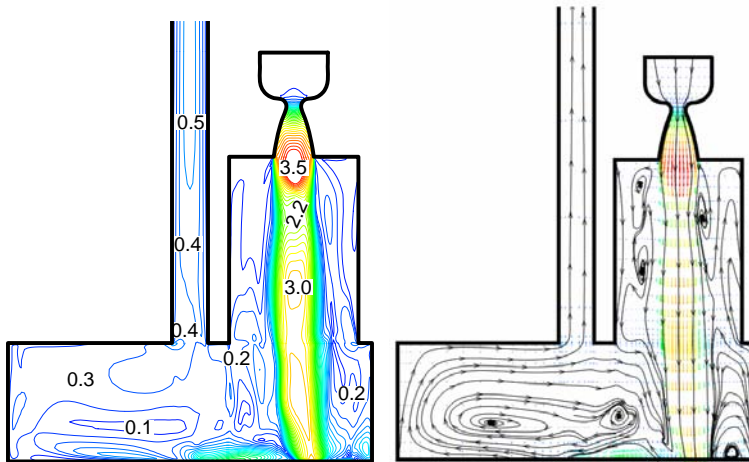
yz-plane



Duct



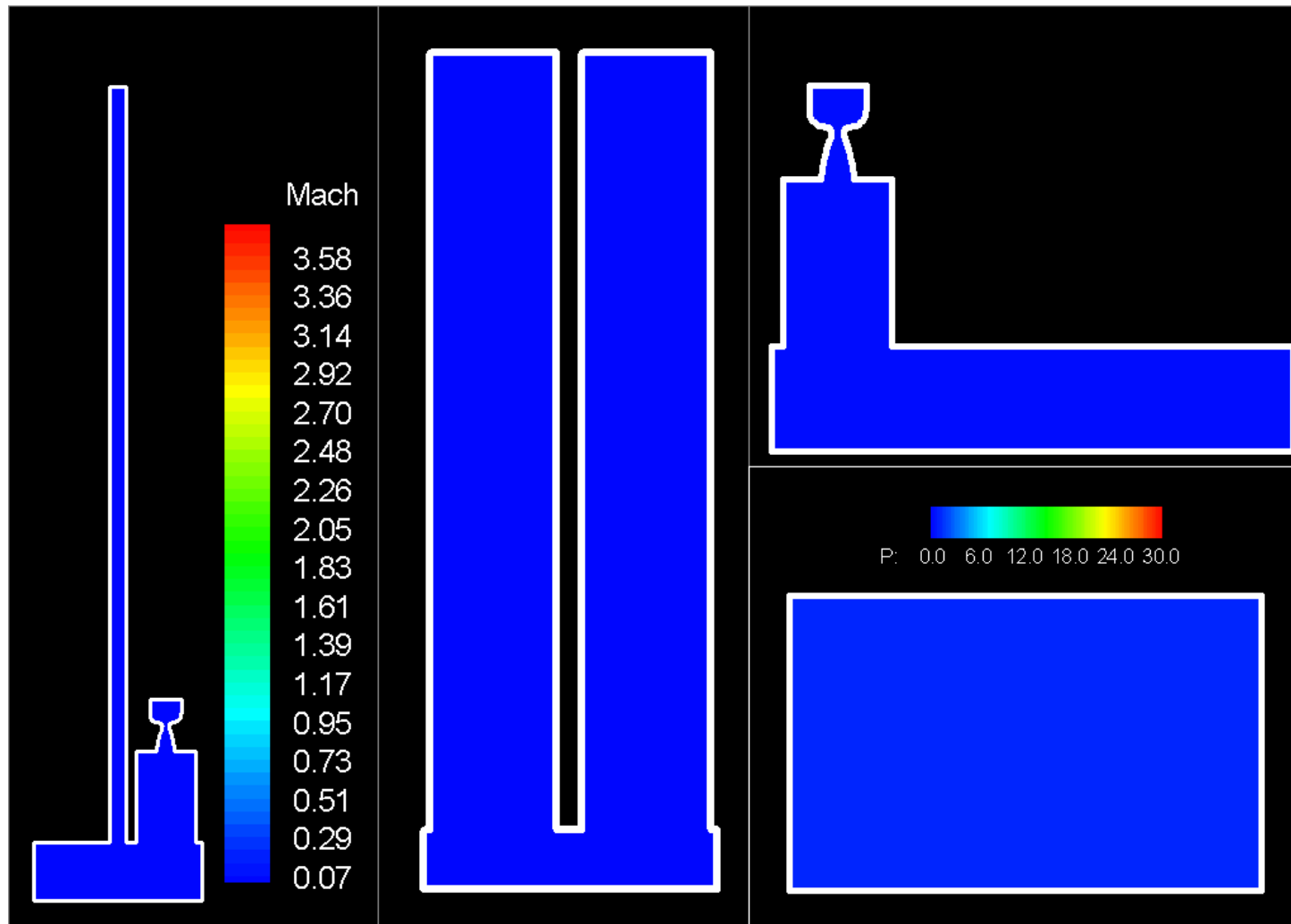
VLS Internal Flow Simulations



Mach Contours and Velocity Vectors of yz-plane



VLS Internal Flow (movie)



Animation of VLS Internal Flow



Frequency Comparison

CASES	H/D	Po (psia)	Dominant Frequency (k Hz)
Test Motor	3	1,200	4.0
	4	1,200	10.1
	5	1,200	8.5
	6	1,200	7.0
Full-Scale Motor	5.4	1,750	20.0
	7.6	1,750	2.8
VLS	7.6	1,750	0.7



VLS Test Fire



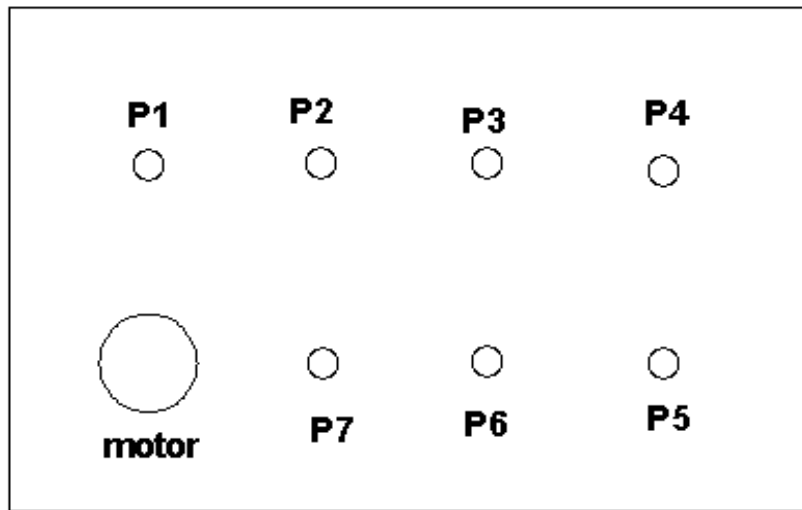
Normal Fire Test



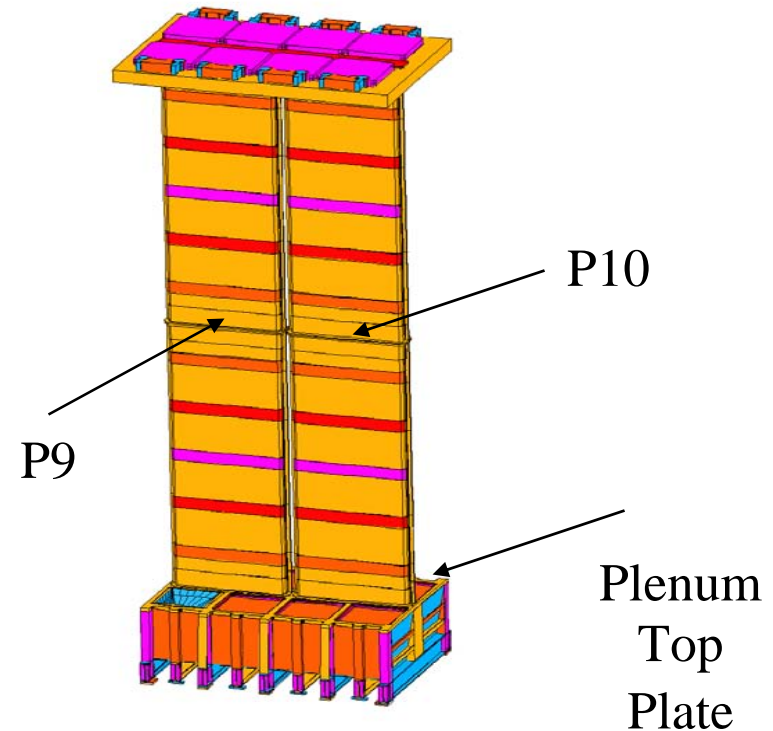
Restrained Fire Test



VLS Test Fire



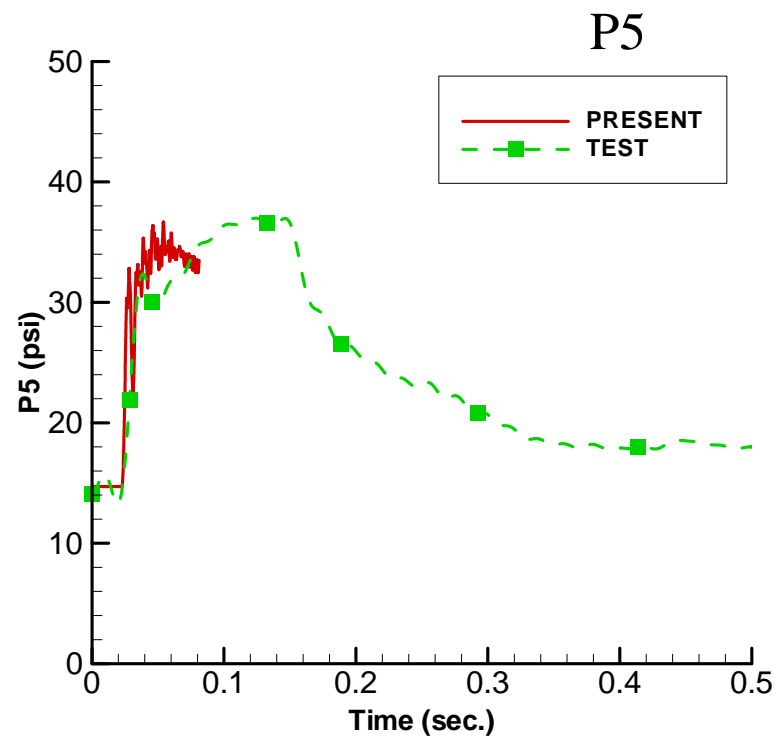
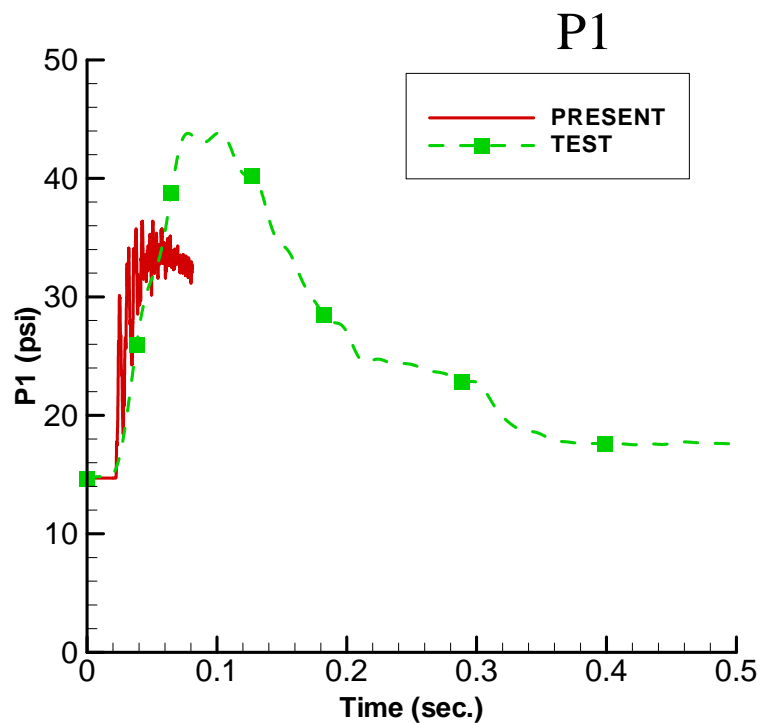
Plenum Top Plate



Sensor Locations of VLS Test Fire



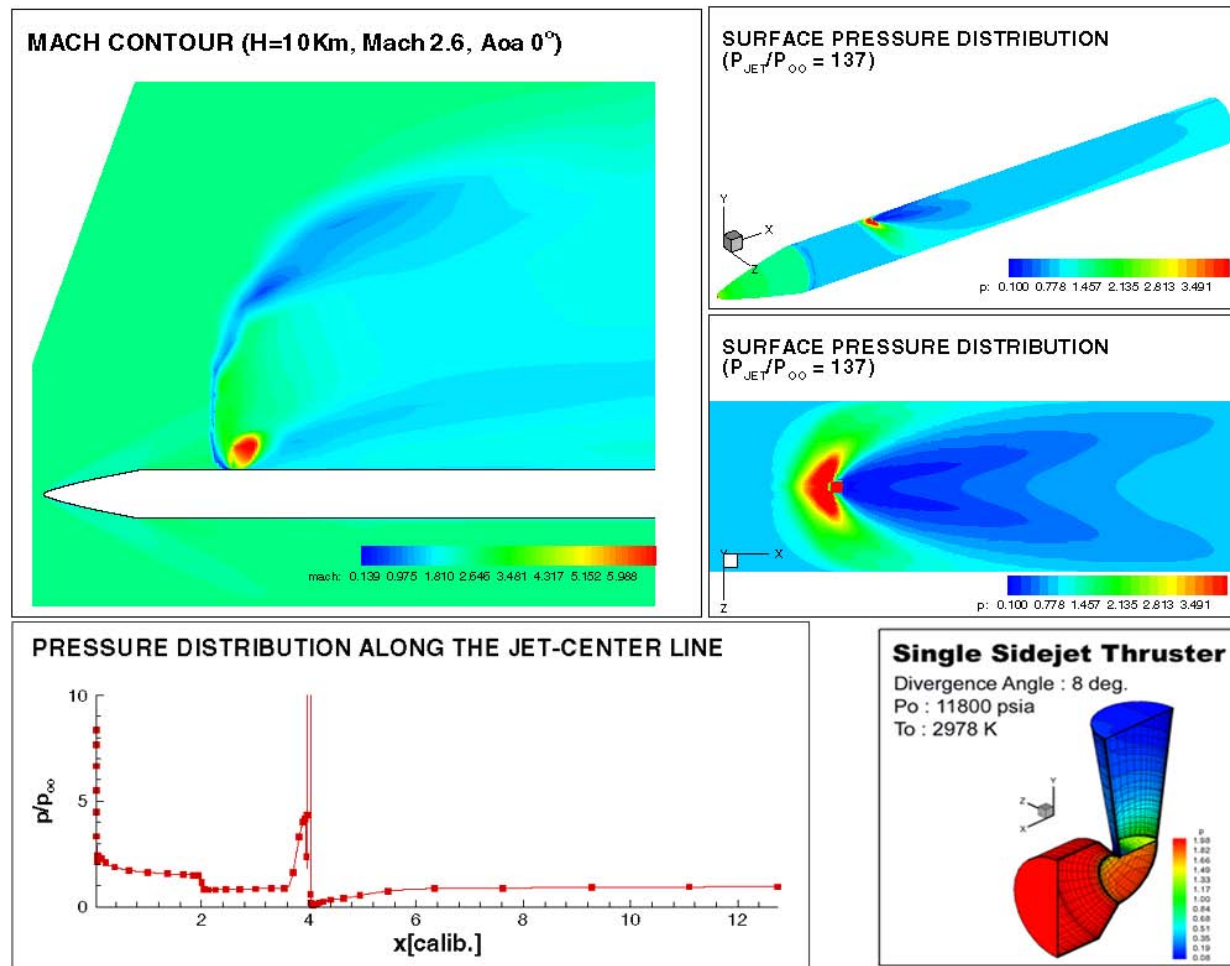
VLS Test Fire



Pressure Comparisons of VLS Flow



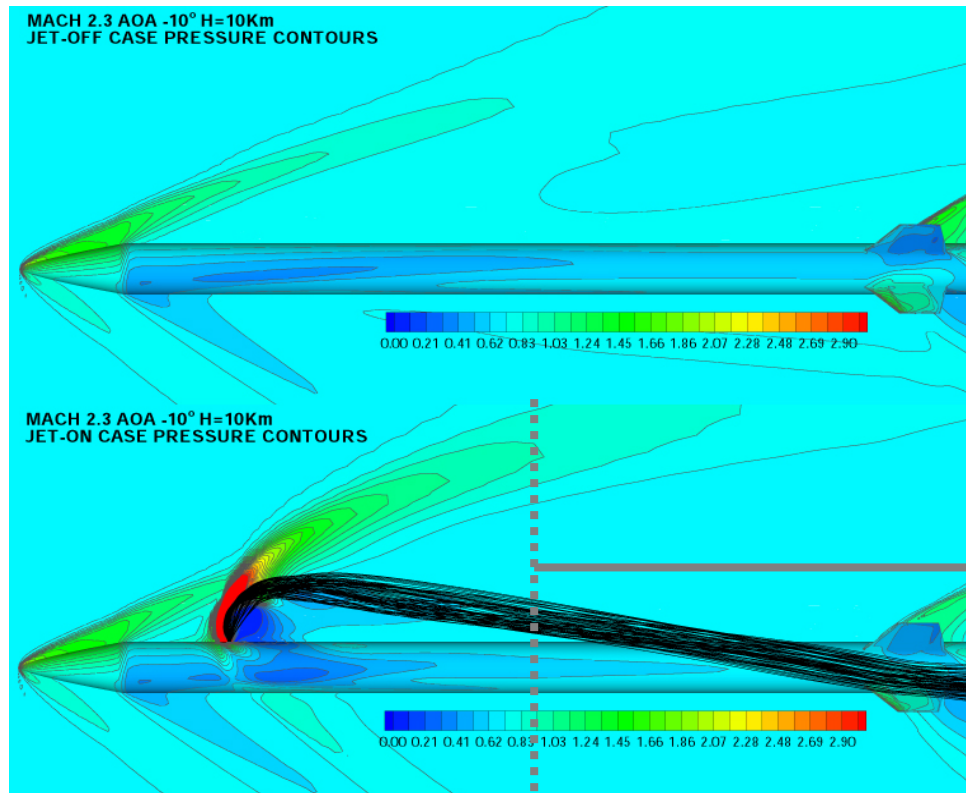
Side Jet Effects on Body-Tail



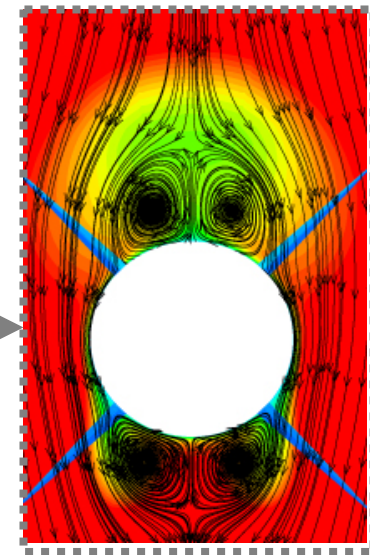
Jet interaction flowfield near and on body surface



Side Jet Simulation



Vortex structure due to body and side jet

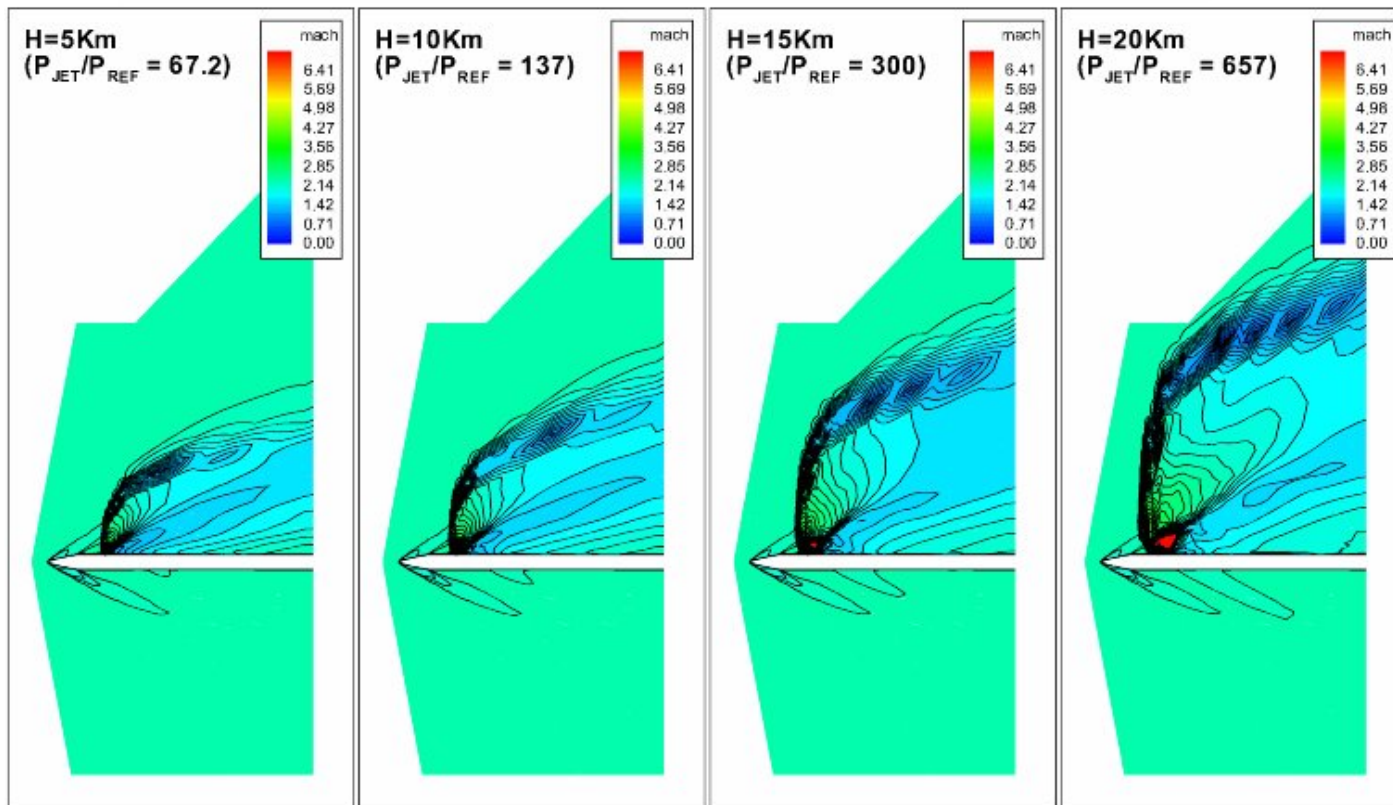


Jet interaction flowfield near and on body surface



Side Jet Simulation

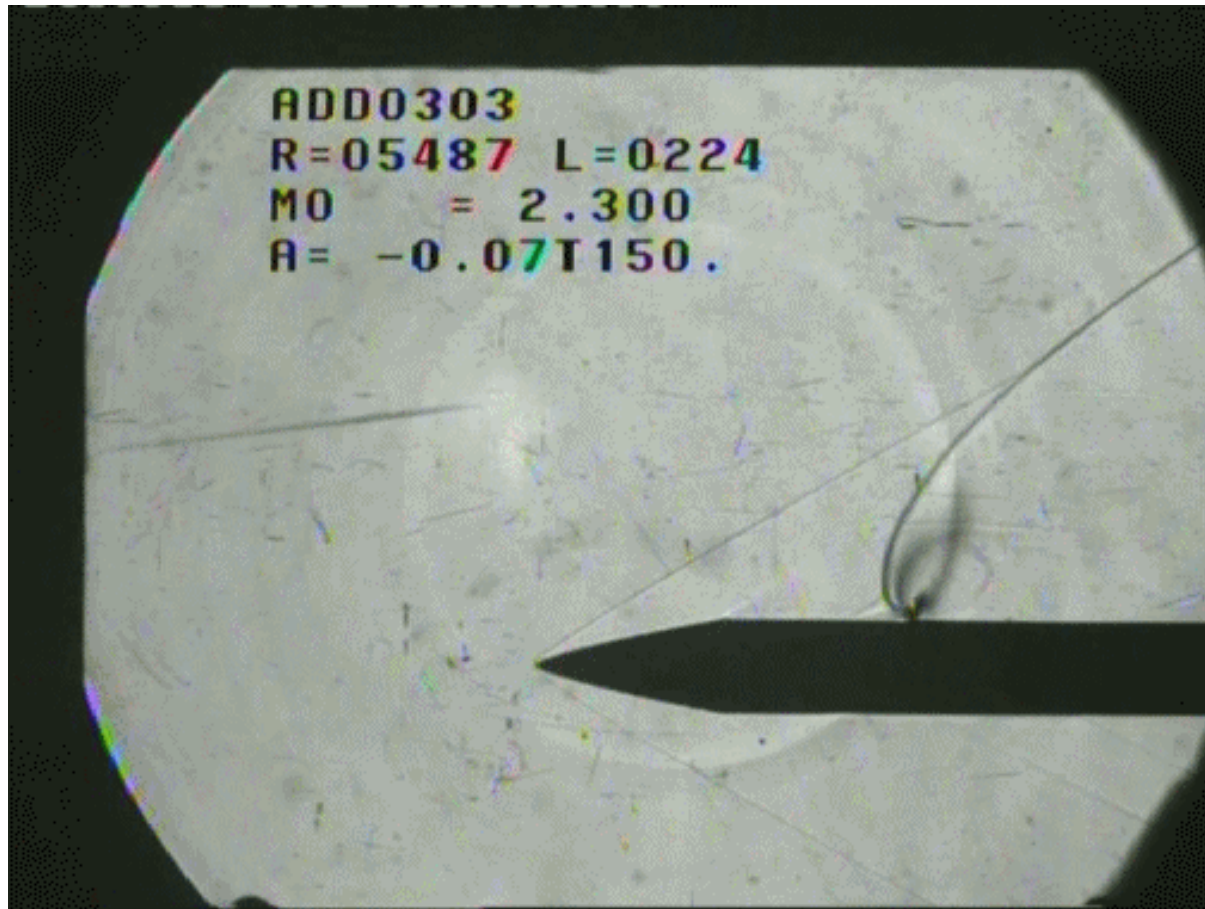
M0102 Body-Alone Computation Results : Aoa=5° Mach 2.3
Single Leeward Jet Cases



Effect of flight altitude on jet interaction



Side Jet Wind Tunnel Test



Side jet wind tunnel test (ONERA Modane)

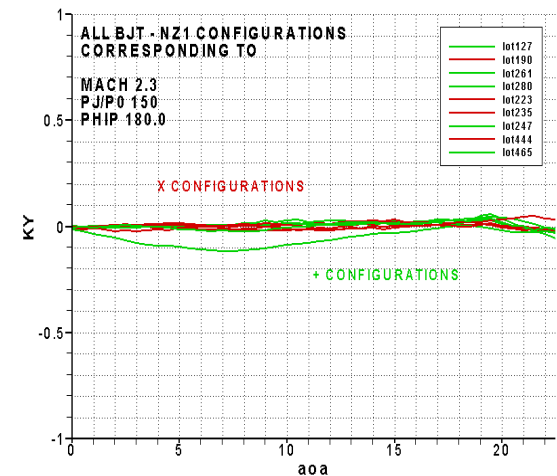
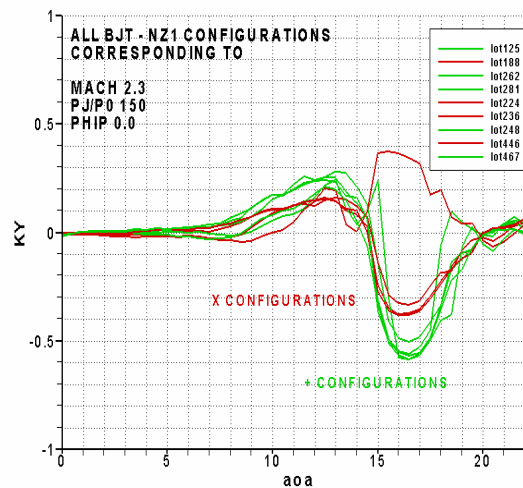
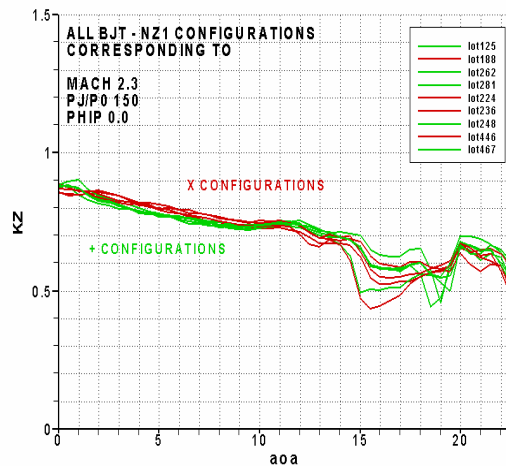


Side Jet Wind Tunnel Test

March-April 2003 France

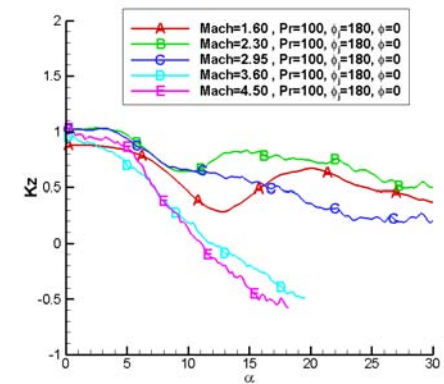
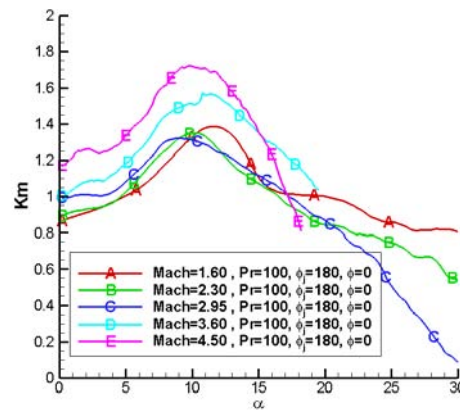
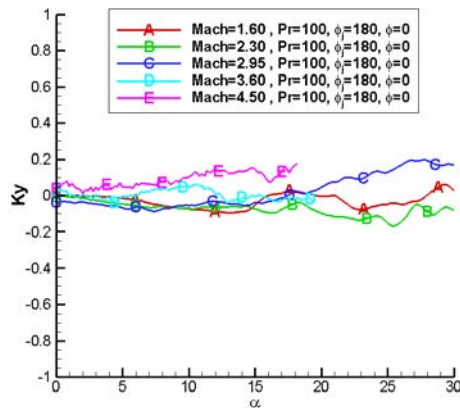
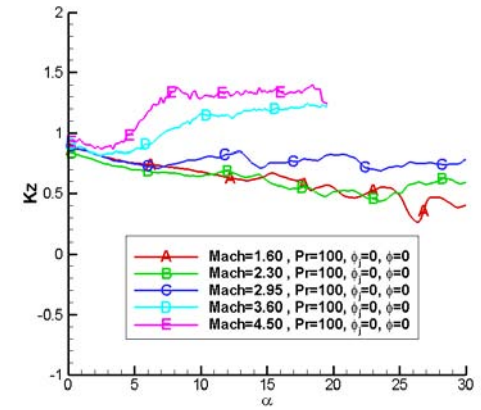
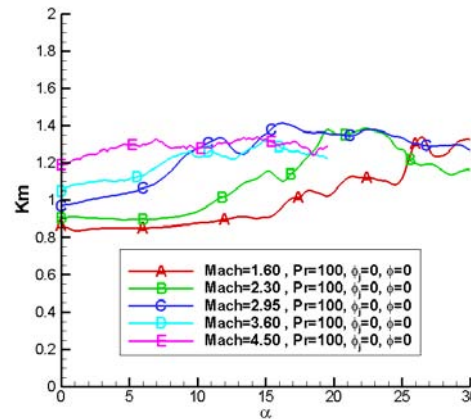
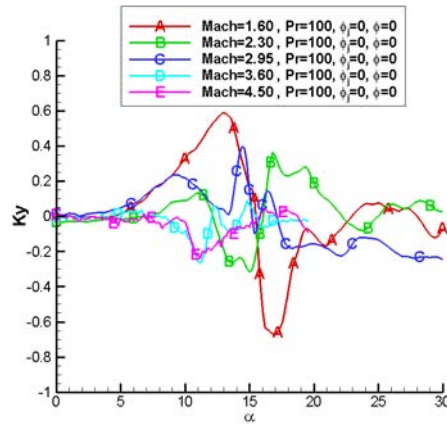
$$C_N = C_{N_{Without\ Jet}} + k_{C_N} N_{Jet} \frac{T_{Single\ Jet}}{Q_{ref} S_{ref}}$$

$$C_M = C_{M_{Without\ Jet}} + k_{C_M} N_{Jet} \frac{T_{Single\ Jet}}{Q_{ref} S_{ref}} \frac{L_{Jet}}{L_{ref}}$$



Side Jet Wind Tunnel Test

April 2007 France



Conclusion

- Aerodynamic design process at ADD is introduced.
- CFD applications for cylinder ogive, boat tail and spike, VLS internal flow, side jet effect, are shown along with validation.
- Various validation techniques are devised for different flows.
- CFD contributes greatly during the missile development phase, giving insight into the flow.
- Coupling with multidisciplinary optimization is our next direction.

